Hierarchical Carbon Fiber Composites with Radially Aligned Carbon Nanotubes: Preservation of In-Plane Tensile Properties

by

Richard Li

Submitted to the Department of Aeronautics and Astronautics
in partial fulfillment of the requirements for the degree of

Master of Science in Aerospace Engineering

at the

MASSACHUSETTS INSTITUTE OF TECHNOLOGY

August 2013
[SEPTEMBER 2013]

Author .....
Department of Aeronautics and Astronautics
August 22, 2013

Certified by .....
Brian L. Wardle
Associate Professor of Aeronautics and Astronautics
Thesis Supervisor

Accepted by .....
Eytan H. Modiano
Professor of Aeronautics and Astronautics
Chair, Graduate Program Committee

Hierarchical Carbon Fiber Composites with Radially Aligned Carbon Nanotubes: Preservation of In-Plane Tensile Properties

by

Richard Li

Submitted to the Department of Aeronautics and Astronautics
on August 22, 2013 in partial fulfillment of the
requirements for the degree of
Master of Science in Aerospace Engineering

Abstract

Hierarchical carbon-nanotube (CNT)-based composites have significant potential to expand the performance and functionality of aerospace composite structures. Notably, circumferentially aligned CNT arrays have previously been grown on woven alumina filaments to form a "fuzzy fiber" reinforced plastic (FFRP) architecture with demonstrated improvements in inter- and intra-ply mechanical properties as well as multifunctional enhancement via tailorable electrical and thermal conductivities. However, thus far, the development of fuzzy carbon fiber reinforced plastics (fuzzy CFRP) with all-around enhanced mechanical properties has been elusive. In particular, prior work attaining growth of CNTs on carbon fibers (CF) have resulted in drastic reductions in fiber tensile strength (e.g., 55% loss), thereby compromising in-plane tensile properties of the resultant fuzzy CFRP. In this thesis, a novel method for high-yield growth of carbon nanotubes on carbon fiber is refined and implemented in the fabrication of unidirectional fuzzy CFRP plies with preserved tensile properties: Non-covalent functionalization of the CF surface coupled with a low temperature thermal chemical vapor deposition process enable high density catalyst adhesion and CNT growth below critical temperatures that would result in fiber strength loss. Successful scale-up to unidirectional fuzzy CFRP specimens with high (67%) and low (32%) CF volume fractions is presented. Testing results indicate that longitudinal elastic properties are retained for all fuzzy CFRP samples consistent with micromechanical analyses. Unexpectedly, the high fiber volume fraction fuzzy CFRP specimens show a 12% decrease in mean tensile strength that was hypothesized to be due to fiber damage introduced through transverse compression during processing of the fuzzy carbon fiber tows. As such, lower fiber volume fraction fuzzy CFRP specimens were subsequently tested and observed to retain strength. These advances pave the way for scale-up to fuzzy CFRP laminates with integrated multifunctionality and improved interlaminar performance without compromising in-plane mechanical properties critical to aerospace-grade composite materials.

Thesis Supervisor: Brian L. Wardle
Title: Associate Professor of Aeronautics and Astronautics

Acknowledgements

I am grateful not only to have had the privilege to conduct this research topic, but also to have received the support of so many people that collectively enabled this work. First and foremost, I would like to thank Professor Brian Wardle, who has been an incredible advisor and coach to me, ever since I was UROP in the basement of building 37. When experiments do not go according to plan, Brian is always there to help offer great insights, connect me with the right resources, and provide invaluable feedback for me to continue to grow as a scientist. Additionally, I want to thank Stephen Steiner for teaching me so much about research and helping me creatively think through tough challenges; Sunny Wicks for the camaraderie and tips in lab during long nights of resin infusion (conveniently documented in this thesis); Peter Florin for the incredible jam sessions and instrumental contributions in developing the presented fabrication processes, Peter Shpik and Mike Kinsella of TohoTenax who generously provided testing materials and important discussions, Mark Payne for taking on the second shift for specimen manufacturing in time for tight deadlines; Jeonyoon Lee for taking on an earlier shift in specimen manufacturing; John Kane for his encyclopedia of hands-on experimental techniques, Ethan Parsons for making sense of speckles on specimens, and many more who have contributed.

Table of Contents

List of Figures

List of Tables

Abbreviations and Symbols

A_c	Cross-sectional area of the composite specimen
A_f	Cross-sectional area of the micro-scale fibers
Ar	Argon
C	Carbon
CF	Carbon fiber
CFRP	Carbon-fiber reinforced polymer (or plastic)
C_2H_2	Acetylene (ethyne)
CO_2	Carbon dioxide
CNT	Carbon nanotube
CVD	Chemical vapor deposition
E_c	Longitudinal composite chord modulus
E_{c_ROM}	Longitudinal composite chord modulus from rule of mixtures
E_f	Longitudinal modulus of fibers
$E_{f\_implied}$	Implied longitudinal modulus of fibers
E_m	Longitudinal modulus of matrix
FFRP	Fuzzy-fiber reinforced polymer (or plastic)
GPa	Gigapascals, 10^9 kg s^{-2} m^{-1} = 10^9 N m^{-2}
H_2	Hydrogen
h-PSMA	hydrolyzed polystyrene-*alt*-maleic acid
HTR-40	TohoTenax high tenacity research-grade carbon fiber
ID	Inner diameter

K-PSMA	Potassium polystyrene-*alt*-maleic anhydride
MPa	Megapascals, 10^6 kg s^{-2} m^{-1} = 10^6 N m^{-2}
MWNT	Multiwall carbon nanotube
N	Nitrogen
n	Number of fibers in tow
nm	Nanometer, 10^{-9} m
OD	Outer diameter
PAN	Polyacrylonitrile
P_{upper}	Load corresponding to the upper strain limit (6000 μstrain)
P_{lower}	Load corresponding to the lower strain limit (1000 μstrain)
r_f	Micro-fiber radius
ROM	Rule of mixtures
sccm	Standard cubic centimeters per minute = cm^3 min^{-1} = mL min^{-1}
SEM	Scanning electron microscopy
SWNT	Single-wall carbon nanotube
V_f (or Vf)	Fiber volume fraction
ε_f	Fiber failure strain
ε_{lower}	Lower strain limit (1000 μstrain)
ε_{upper}	Upper strain limit (6000 μstrain)
μm	Micron (or micrometer), 10^{-6} m
$\sigma_{cmaxROM}$	Tensile strength of composite as determined from ROM
σ_{fmax}	Tensile strength of fibers
$\sigma_{f\_implied}$	Implied fiber tensile strength
$(\sigma_m)_{\varepsilon f}$	Matrix in matrix at fiber failure strain

Chapter 1

Introduction

1.1. Motivation

In the face of global climate change and increased economic pressures to reduce anthropogenic greenhouse gas emissions, lightweight structural materials are touted for their potential to usher in a new generation of fuel-efficient transportation. The aerospace sector in particular, has made dramatic leaps into increased use of heterogeneous materials, which matches property advantages of constituents to suitable loading conditions (e.g., sandwich structures), resulting in overall vehicle mass reductions. Notable examples include the Boeing 787 and Airbus A350, in which an unprecedented majority of a passenger aircraft is composed of filamentary composite materials. In these and other aviation instances, carbon fiber reinforced plastic (CFRP) laminates are heavily utilized, as such materials synergistically combine strong and stiff, yet low-density graphitic filaments with a polymer matrix. The laminated architecture also allows for the elastic response tailoring through ply orientation stacking sequences, expanding its versatility to a variety of structural applications.

However, to push the performance envelope even further, there are still many opportunities for composite advancements, especially in matrix-

dominated properties. Delamination resistance and integrated lightning strike protection are crucial capabilities still to be attained. As a result, the incorporation of nano-fillers, such as carbon nanotubes (CNTs), with high strength and electrical conductivities, is of great interest in order to address these shortcomings without altering the existing micro-scale architectures critical to CFRP performance. A nano-engineered composite architecture of primary focus in this study integrates radially aligned carbon nanotubes (CNTs) on composite fiber surfaces, yielding a "fuzzy fiber" reinforced plastic (FFRP) that has inter and intra-laminar reinforcement as well as increased electrical and thermal conductivities. Prior FFRP implementation on alumina fiber composites have empirically characterized these mechanical and multifunctional enhancements, motivating the same implementation onto aerospace CFRP. However, research attempts for circumferential growth of CNTs on CF has been met with significant challenges such as low CNT yield and large degradation in fiber tensile properties [3].

Recently, work conducted by Steiner et. al. has demonstrated high yield CNT growth on CF substrates while preserving single filament strengths and modulus [2]. These novel methods employ a simple yet innocuous wet chemistry procedure for catalyst adhesion onto fiber surfaces, and much lower temperature chemical vapor deposition (CVD) process for CNT growth. As such, it holds great promise for scalability to fuzzy carbon fiber reinforced plastics (fuzzy CFRP) with uncompromised tensile properties, and is of great interest for further study in this thesis.

1.2. Outline

The primary goal of this thesis is to develop, test, and assess in-plane tensile properties of ASTM compliant ply-level fuzzy CFRP specimens that

were fabricated from fuzzy carbon fibers with retained strengths (per one of the methods presented by Steiner et. al.).

Chapter 2 will provide an overview of previous work with composite reinforcement through nano- and micro-scale architectures, and focus on the advances within the FFRP architecture. Challenges of CNT growth on CF and developed strategies will be discussed. Chapter 3 outlines the specimen fabrication steps starting with refinement of CNT growth on CF tows, proceeding to impregnation techniques, and ending with the final testing methodology. Previous processing trials and key parameters will be highlighted. Chapter 4 presents tensile testing results on longitudinal modulus and breaking strength. Additionally, experimental data is compared with micromechanical predictions. Chapter 5 summarizes the primary contributions from this work, and suggests immediate and future work. In particular, a host of potential materials characterizations for laminate-level fuzzy CFRP samples will be of great value towards aerospace applications.

Chapter 2

Background

Advanced nano-engineered composites have potential in addressing the shortcomings of aerospace composites and integrating multifunctional enhancements into the material. In particular, radially aligned carbon nanotubes on micro-scale fiber architectures are desired for their demonstrated improvements in mechanical, electrical, and thermal properties. The section discusses the motivation, key challenges, and recent advances of such architectures with carbon micro-scale fibers.

2.1. Fiber-Reinforced Plastics

Fiber-reinforced composite materials are increasingly being used within the aerospace industry as it enables lighter weight yet higher performing structures. Essential to its performance are two constituents: a micro-fiber with high specific stiffness/strength, and a low density compliant polymer matrix. Typically, a 2D laminated architecture is used to combine these two materials, where layered fiber plies (dry or pre-impregnated) are stacked and held in place by the matrix. Whereas brittle fibers serve to carry the majority of the load in the longitudinal direction of a ply or laminate, polymer matrices effectively transfer load around fiber breakage. Thus a synergistic effect results, in which the combination of the two materials result in a composite

with mechanical properties better than that derived from a volume weighted average. [4]

Many types of composites are in wide use for structural applications today including Kevlar/epoxy, graphite/epoxy typically known as carbon fiber reinforced plastic (CFRP), fiberglass/epoxy (glass fiber reinforced plastic, GFRP), and carbon/carbon. CFRP laminates are the most commonly used within aerospace, in particular due to the high performance of ex-PAN carbon fibers that have strengths of ~4 GPa and stiffness in excess of 200 GPa [5], as well as low coefficients of thermal expansions critical to some applications such as satellite panels. Additionally, anisotropic behavior can be engineered into the composite based on stacking sequences of differing ply angles. For instance, bending/twisting coupling could be designed into wing surfaces to passively change angle of attack under increased load, thus creating an optimized and/or larger flight envelope [6].

Despite the advantageous in-plane performance of CFRP laminates, matrix-dominated interlaminar properties can still be improved. Because plies are held together only by resin, these inter-ply regions are typical points of delamination, which is commonly initiated from impact, fatigue, or large out-of-plane loadings. As a result, much effort in the past has focused on through-thickness micro-scale reinforcement strategies. One such technique is z-pinning, in which 0.2 - 1.0 mm diameter metal or fibrous pins are (ultrasonically) driven through a layup of dry or uncured prepreg preforms. Typical resultant z-pin volume fractions amount to 0.5% to 4.0% (8-70 z-pins/cm^2), with reported doubling of mode I toughness increases for every 0.5% increment in z-pin volume fraction [7]. 3D stitching is another technique in which high strength threads such as Kevlar are sown through stacked plies or even multiple components. CFRP Mode I toughness was observed to increase 8 fold with a stitch density of 7 stitches/cm^2 [8]. In addition, 3D

woven and braided CFRP have carbon fiber tows that run along the through-thickness direction, and were thus found to have better delamination resistance than 2D laminates. However, common among these methods are the large compromises observed for in-plane properties. Z-pin insertions often rupture adjacent fibers, and create crack initiation sites, such that a 60% loss in CFRP tensile strength can arise from a 10% pin volume fraction. Likewise, fiber distortion and breakage in 3D stitching degrades both tensile modulus and strength by as much as 20%. Meanwhile, weaving-induced damage onto low-bearing tows and pinching of surface tows can cause 50% strength loss for 3D woven composites. Therefore, because large-scale reinforcements alter existing fiber architectures, in-plane strengths are traded for through-thickness property improvements [8].

2.2. Nano-Engineered Composites

The integration of nano-fillers (nano-scale particles or fibers) into matrices is a promising concept to improve the interlaminar and (and perhaps intralaminar) properties of laminated composite for several key reasons. First, nano-scale fibers have the potential to serve as reinforcing filaments within a polymer, and effectively create a toughened and strengthened matrix for a micro-fiber composite. Secondly, the length-scales of nano-materials are appropriate for full integration in between composite filaments, thereby enabling matrix reinforcement between fibers and plies without distorting fiber architectures. Additionally, multifunctional attributes can be built into matrices by selecting nano-fillers with desired thermal or electrical characteristics, and incorporating them at targeted volume fractions/ morphologies. Many types of nano-fillers have been experimented in polymers, but one of particular value for epoxies are carbon nanotubes

(CNTs). Since its identification by Iijima *et al.* [9], CNTs - rolled graphene sheets that appear as single-walled nanotubes (SWNT) or multiwalled nanotubes (MWNT) - have been of interest as structural materials due to their high theoretical strength (up to 63 GPa for arc-MWNT), stiffness (up to 950 GPa for outer-wall), and aspect ratio [10]. These properties are particularly attractive to maximizing pull-out energies of CNTs from polymer, which is a dominant matrix toughening mechanism [11-14]. High electrical conductivity of CNTs has also been demonstrated to dramatically reduce epoxy resistivity in aligned carbon nanotube polymer composites (A-PNCs) [15], suggesting that a conductive composite matrix with integrated electromagnetic interference shielding or lightning strike protection may be attainable through CNT integration.

To assess CNT-toughening effects within micro-fiber composite specimens, many different CNT integration techniques have been employed. In one primary method, CNTs are dispersed within polymer prior to infusion, and found to improve interlaminar shear strength slightly by 5% with a 1% CNT volume fraction [16]. While properties can be improved with higher CNT volume fractions, a host of processing issues such as increased resin viscosity, CNT agglomerations/clustering due to van der Waals forces, and uneven dispersion from fabric filtration effects places a low practical limit. An attractive approach that avoids dispersion processing limitations is the fuzzy fiber reinforced plastic architecture (FFRP), in which radially aligned CNTs are grown circumferentially on the fibers surfaces prior to impregnation. This hybrid architecture allows for both inter- and intra-ply reinforcement, as well as control for location and orientation of CNT arrays. Typical aligned multi-walled CNT (MWCNT) growths can be achieved on fibers utilizing a thermal chemical vapor deposition (CVD) process. Fiber substrates are first pre-deposited with typical metallic catalyst particles (Co, Ni, and Fe) and then

heated to ~700°Celsius [17]. Carbon-containing gases - usually ethylene or acetylene - are introduced to the fibers, resulting in decomposition of the hydrocarbon, dissolution of carbon onto the catalytic nanoparticles, and precipitation of carbon around the particle surface in the form of hollow nanotubes. In certain instances, catalysts are deposited onto the fabric in the CVD environment through upstream injections at high temperatures (floating catalyst CVD processes) immediately prior to introduction of carbonaceous species. Aligned CNT growth was achieved through this manner on SiC weaves by Veedu *et al.* [18], but was limited to the surfaces of the cloth exposed to catalysts. On the other hand, conformal growth around micro-fibers was attained through dip-coating alumina woven fabric within 0.05M $Fe(NO_3)_3 \cdot 9H_2O$ in isopropanol catalyst solution as demonstrated by Wardle *et al.* [1, 19]. Notably, subsequent characterization of these alumina/epoxy FFRP specimens revealed over 75% increase in steady-state mode I toughness [19], 69% increase in interlaminar shear strength [1], and 9% improvement in tension bearing strength [19]. An experiment-model correlation was demonstrated between empirical toughness values with a closed-form solution of perfectly aligned CNTs at the interlaminar interface [11, 20]. Further, both in-plane and out-of-plane electrical conductivities were enhanced by several orders of magnitude (effectively turning insulating alumina/epoxy into conductive specimens) while out-of-plane thermal conductivity was doubled [21]. Thus, the FFRP architecture bears significant potential for integrating mechanical and multifunctional enhancements into laminated composites, and is highly desired for implementation on aerospace CFRP.

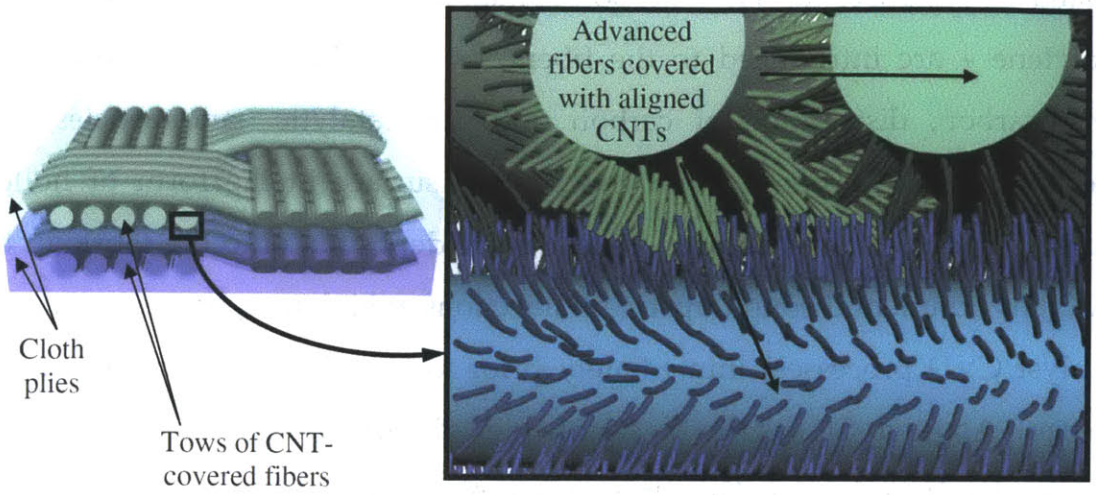

Figure 2.1 Schematic illustration of the Fuzzy Fiber Reinforced Plastic (FFRP) architecture. CNTs circumferentially coat individual filaments of a cloth *(right)*. Cloths containing CNT covered fiber tows can be laid up as composite plies in a polymer matrix *(left)* [1].

2.3. Challenges of Growing CNTs on CFs

Whereas high yield and radially aligned CNT arrays were demonstrated on alumina fibers (in alumina FFRP) without reducing fiber properties [22], the same could not be easily achieved on carbon fibers. Qian *et al.* observed a 57% increase in fiber-epoxy interfacial shear strengths (IFSS) by growing unaligned CNTs on CFs, but found a 55% loss in fiber tensile strength. Steiner *et al.* achieved nearly aligned CNT growths on alumina sol-gel coated CF, but a reduction of 53% in mean tensile strength [23]. Zhang *et al.* examined CVD processing effects on Fabric Develop Inc. T650 fibers, and concluded no significant strength loss resulted. However, closer examination of their strength plots reveals a large variation (coefficient of variation ~ 30%) in tensile strength data, and an observed decrease of ~40 % in average tensile strength for processed T650 fibers [24]. Sager *et al.* also used a floating catalyst CVD process for growing MWCNT on unsized T650, and observed fiber

tensile strength loss of 37% [25]. Evidently, carbon fiber tensile properties are compromised when traditional CVD processes are utilized to grow CNTs, creating a barrier to fuzzy CFRP laminates as discussed in a review of fuzzy fiber composite [26, 27]. Hence, while interlaminar properties of CFRP may be improved from subjecting fibers to these CNT growth methods [28], in-plane tensile properties will be sacrificed.

To circumvent this apparent tradeoff in mechanical properties, further understanding the origins of carbon fiber strength loss was necessary. As one challenge, metal CNT growth catalysts dissolve carbon surfaces at the high temperatures normally used for CNT growth. In fact, Qian *et al.* observed pitting on fiber surfaces once nanotubes and catalysts were removed after CVD processing. Additionally, graphitic CF surfaces typically have poor wettability to catalyst solutions, causing prior work to resort to surface etching techniques or barrier approaches prior to dip-coating in catalyst solution [3]. Since loads on an ex-PAN carbon fiber are primarily carried on the outer surface of the fiber, minor surface defects can trigger drastic strength loss [29] (i.e., surface modifications must be avoided). As a result, Steiner *et al.* employed barrier coatings on unsized HTR-40 carbon fibers prior to catalyst loading in an effort to prevent fiber surface dissolution. However, tensile strength loss was still evident, and a parametric study revealed that the largest contribution to strength loss (-37%) was attributed to heating uncoated carbon fibers to CNT growth temperatures [23]. In fact, subsequent work found that even in inert atmospheres, a critical temperature exists between 400°C and 650°C, above which fiber strength loss occurs [2]. Thermogravimetric analysis revealed a significant chemical event at ~550°C, and Auger Spectroscopy detected chemical composition changes (e.g., N/C ratios) with increased heat treatment temperatures. From the above considerations, Steiner *et al.* determined two critical requirements for high

yield CNT growth CF that preserves tensile properties: 1. A non-covalent functional coating on CF that would allow catalyst adhesion without direct fiber-catalyst contact; and 2. Low temperature CNT growth below the determined strength loss temperature ~550°C [2].

Previous work by Carrillo *et al.* revealed that a hydrolyzed polystyrene-*alt*-maleic anhydride (h-PSMA) polyelectrolyte could be used to functionalize graphitic surfaces with carboxylic acid groups [30]. Meanwhile, Magrez et al reported CNT growth on a variety of carbon substrates at temperatures as low as 400°C [31]. Modifying and integrating these two aforementioned methods, Steiner *et al.* first engineered a potassium polystyrene-*alt*-maleic anhydride (K-PSMA) coating that non-covalently adsorbs to the fiber surface, leaves external potassium ions available for exchange with Fe^{3+}, thereby catalyst particles separated from the fiber surface. Additionally, a low temperature CO_2/C_2H_2 CVD process was implemented at a corrected temperature of 480°C, to allow CNT growth on coated fiber substrates. Indeed, after these strategies were applied to carbon fiber tows, conformal and high-coverage CNT growth was evident throughout the tow (Figure 2.2). More importantly, single filament testing [32] showed that CNT-coated CFs have preserved tensile strengths (Figure 2.3).

This advance enables high-yield growth of CNTs on high performance CF without degrading tensile properties, and makes possible a carbon-fiber based FFRP (fuzzy CFRP) without compromise to existing mechanical properties. As the next step, this thesis aims to contribute the first scale-up to ply-level fuzzy CFRP specimens, and provide tensile testing data crucial to developing hierarchical aerospace composites with preserved in-plane properties.

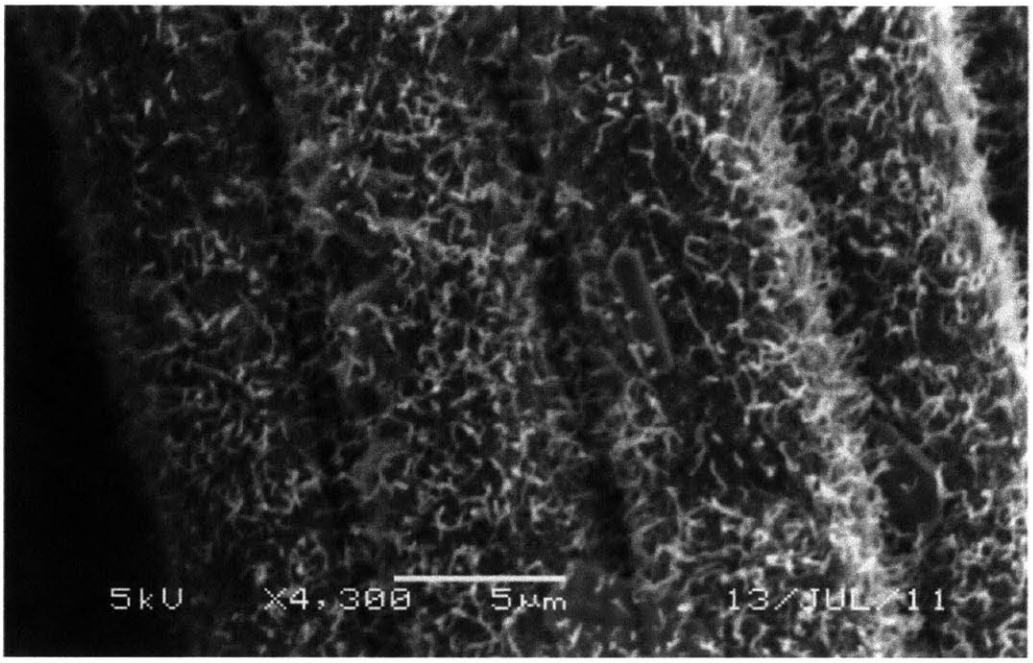

Figure 2.2 SEM image of CNTs grown on unsized HTR-40 carbon fibers that were coated with K-PSMA/ Fe^{3+} catalyst and subjected to 480°C CO_2/C_2H_2 CVD processing [2].

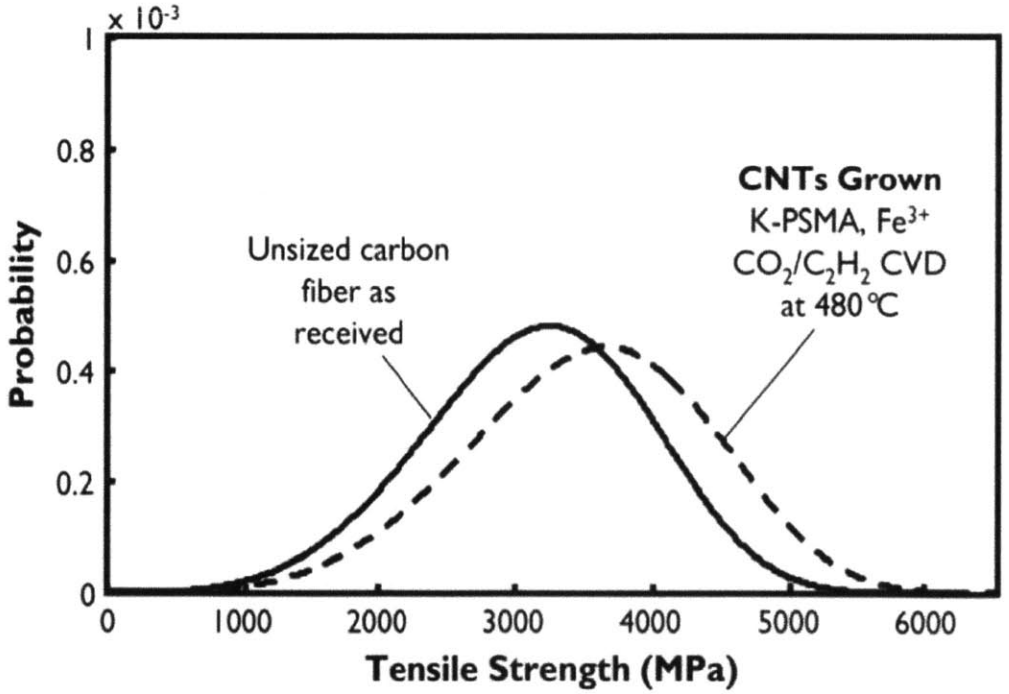

Figure 2.3 Unsized HTR-40 and CNT coated HTR-40 (fuzzy CF) carbon fiber single filaments were tested, fitted to a Weibull distribution at a fixed 25 mm gauge length, and plotted here [2].

Chapter 3

Fabrication and Testing

In order to assess the in-plane tensile properties of fuzzy CFRP, a process for CNT growth on carbon filaments [2, 33] was refined, and an impregnation system was developed to manufacture carbon fuzzy fiber reinforced specimens (fuzzy CFRP) at targeted fiber volume fractions. This section discusses the incipient-wetting processing refinements, the impregnation procedures, and tensile testing specimen fabrication.

3.1. Growth and Dip-coating Optimization:

3.1.1. Dip-coating Studies

Prior work in attaining radially aligned CNT growth on carbon fiber yielded two approaches that enable the preservation of carbon fiber strength [2]: Tension of filaments during CVD processing, and an integration of low temperature CVD and non-covalent functionalization. While the efficacy of the former was demonstrated by tensioning individual carbon fiber filaments on a graphitic apparatus subjected to typical CNT growth conditions (ethylene, helium, and hydrogen at 650°C), repeating the treatment to all filaments in a tow would necessitate intricate tow spooling and tension monitoring devices that would be challenging to fit within existing

laboratory-scale tube furnace CVD systems. More importantly, because fibers are tensioned over rollers in industrial production to tailor resultant filament properties [34], the first approach is well-matched to a continuous line and will attain strength preservation once implemented at full scale. Hence it is of greater interest to conduct this work utilizing the second aforementioned method.

Figure 3.1 is a depiction of this integrated approach for attaining aligned CNTs on CF. Unsized TohoTenax HTR-40 carbon fibers are first dip-coated in a functional coating of potassium polystyrene-*alt*-maleic anhydride (K-PSMA), which circumferentially adsorbs onto the fiber surface and leaves potassium ions free for ion exchange with Fe^{3+} upon subsequent immersion in catalyst solution. The crucial advantage for this non-covalent system is that it supports high-density catalyst adhesion without acid etching and harmful modifications of the fiber surface, critical to PAN-based carbon fiber strengths as discussed earlier. Fe^{3+}/KPMSA coated fibers (in tow form) can then be placed inside a CVD tube furnace, and subjected to a low temperature CNT growth at 480°C, which is significantly lower than traditional CVD processing at 730°C. More importantly, this CO_2/C_2H_2 oxidative dehydrogenation reaction [31] occurs below the critical temperature of ~550°C, above which fiber strength loss was observed even in inert atmospheres [2].

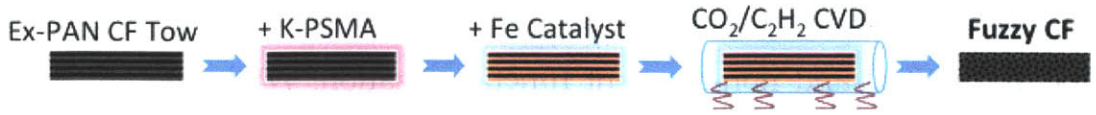

Figure 3.1 Procedure for growing CNTs on CF without degrading filament strength. Ex-PAN fibers are non-covalently functionalized in K-PSMA coating, dip-coated in iron nitrate solution, and subjected to CO_2/C_2H_2 thermal CVD at 480°C for CNT growth. Resultant tows have circumferential CNT growth around each fiber.

The integrated low temperature CVD and non-covalent functionalization approach was further refined to improve alignment, density, and coverage of the CNTs on the carbon fibers. Many variables ultimately affect iron catalyst nanoparticle sizes desirable for densely aligned growth on the CF surface. A parametric study was conducted to explore the individual effects of coating concentration, catalyst solution mixing time, catalyst solution solvent type, drying conditions, and K-PSMA batches.

Initial SEMs of trials employing dip-coating with 1.5 wt. % K-PSMA revealed evidence of thick K-PSMA aggregates wicking in between fibers, and prominent cracking of the coating in between filaments where capillary wetting is dominant. As a result, a thinner and uniform functional coating was desired to allow for higher volume fractions to be attained with packing of fuzzy carbon fibers, which have higher effective fiber diameters due to the radial CNTs than baseline CFs. K-PSMA was modified by preparing 0.5 wt. % h-PSMA as outlined in Strook *et al.* [35]: 1.4 grams of Polystyrene-*alt*-maleic anhydride (Sigma-Aldrich, 99%, Molecular weight of 350,000) was dissolved in 25 mL of acetone facilitated by stirring and light heating. This solution was slowly mixed with 300mL of 0.3M aqueous sodium hydroxide and then stirred for 3 hours. 0.1M nitric acid was then added to bring the pH down to 8 and acetone was removed from the solution using a rotary evaporator. K_2CO_3 was added until the solution pH reached 11. Afterwards, 0.25 wt. % K-PSMA solution was prepared by adding deionized water equivalent to solution mass. SEM images show that coating thickness is visibly decreased with lower solution concentration without greatly reducing forest density (Figure 3.2).

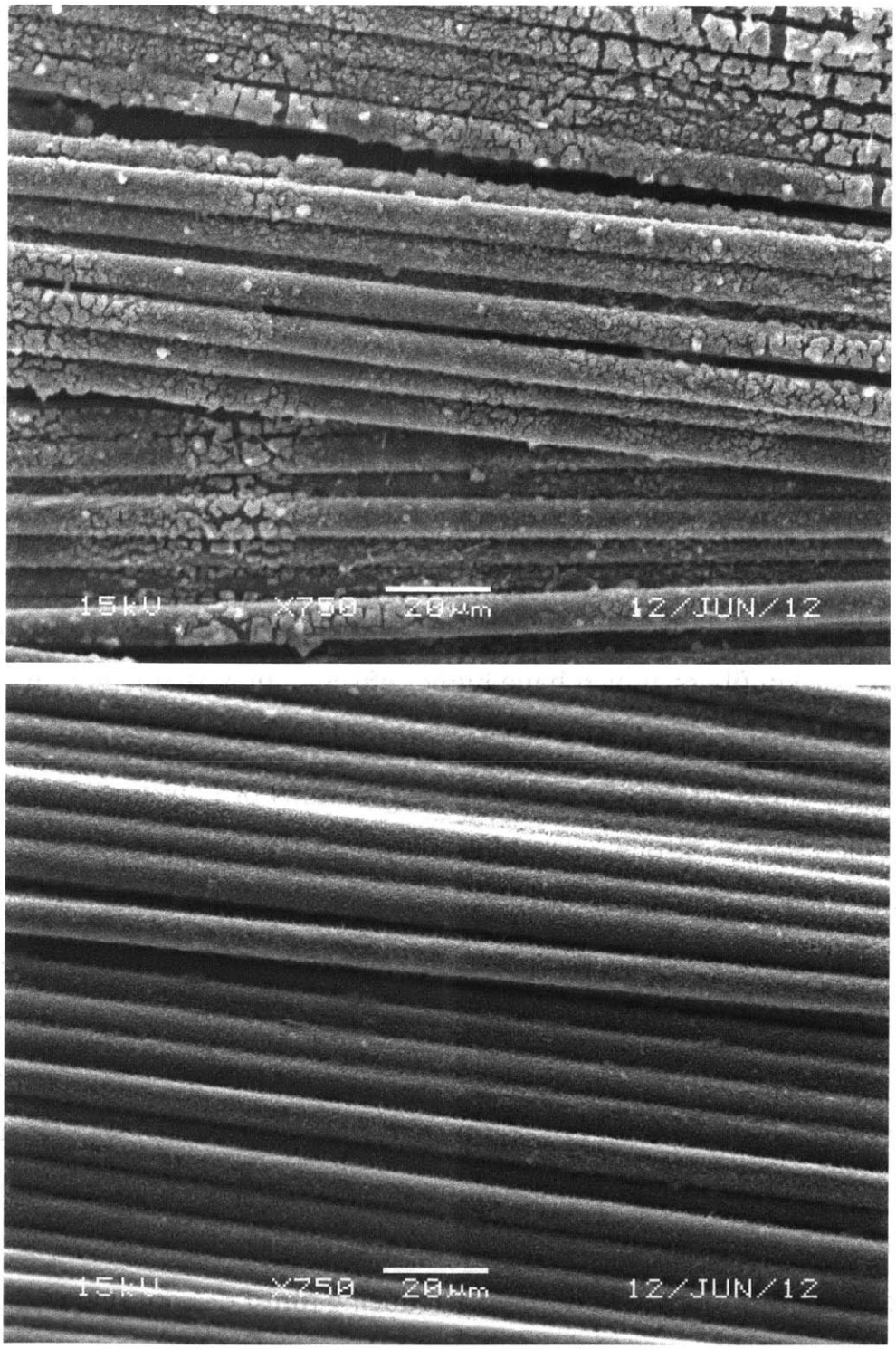

Figure 3.2 Fe^{3+}/0.5 wt. % K-PSMA coated and CVD processed HTR-40 fibers have residual coatings that are prone to cracking at high K-PSMA concentrations that give thicker coatings *(top)*, Fe^{3+}/ 0.25 wt. % K-PSMA coated and CVD processed HTR-40 fibers have thinner and more conformal coatings/CNT growth *(bottom)*.

Contrary to 0.05 M $Fe(NO_3)_3 \cdot 9H_2O$ aqueous solutions, 0.05 M $Fe(NO_3)_3 \cdot 9H_2O$ in isopropanol consistently yielded CNT growth. Catalyst solution mixing time is a critical parameter as explored in previous literature [33, 36]. An optimal mixing time exists below which iron oxide nanoparticles in solution are too small and dilute for uniform aligned growth, and above which, coarser catalyst particles would form carbon nano-fibers (the dependency of CNTs thickness on substrate deposited catalyst particle diameters was observed). It was found that a mixing time of 60 minutes yielded desirable CNT morphologies.

Additionally, drying conditions were found to have a significant effect on both the resultant CNT morphologies. Large variability in catalyst wetting was evident during the preliminary studies done under Steiner *et al.*'s work in which tows were left to dry in front of fan overnight subjected to ambient conditions. Samples that were left to dry inside a sealed container resulted in virtually no growth upon low temperature CVD, and also fatter "nano-fibers" as opposed to CNTs (figure 3.3). These results indicate that a lower vapor pressure and a more controlled evaporation of isopropanol from the carbon fiber surface is desirable for smaller catalyst particles, and thus the desired small diameter CNTs. Consistent with longer iron nitrate mixing times, it was hypothesized that longer isopropanol evaporation times tend to result in aggregation of catalyst particles, and thus wider nanotubes. As a result, a vacuum heating drying procedure was developed on carbon fiber tows while being subjected to low tension to maintain collimation of filaments.

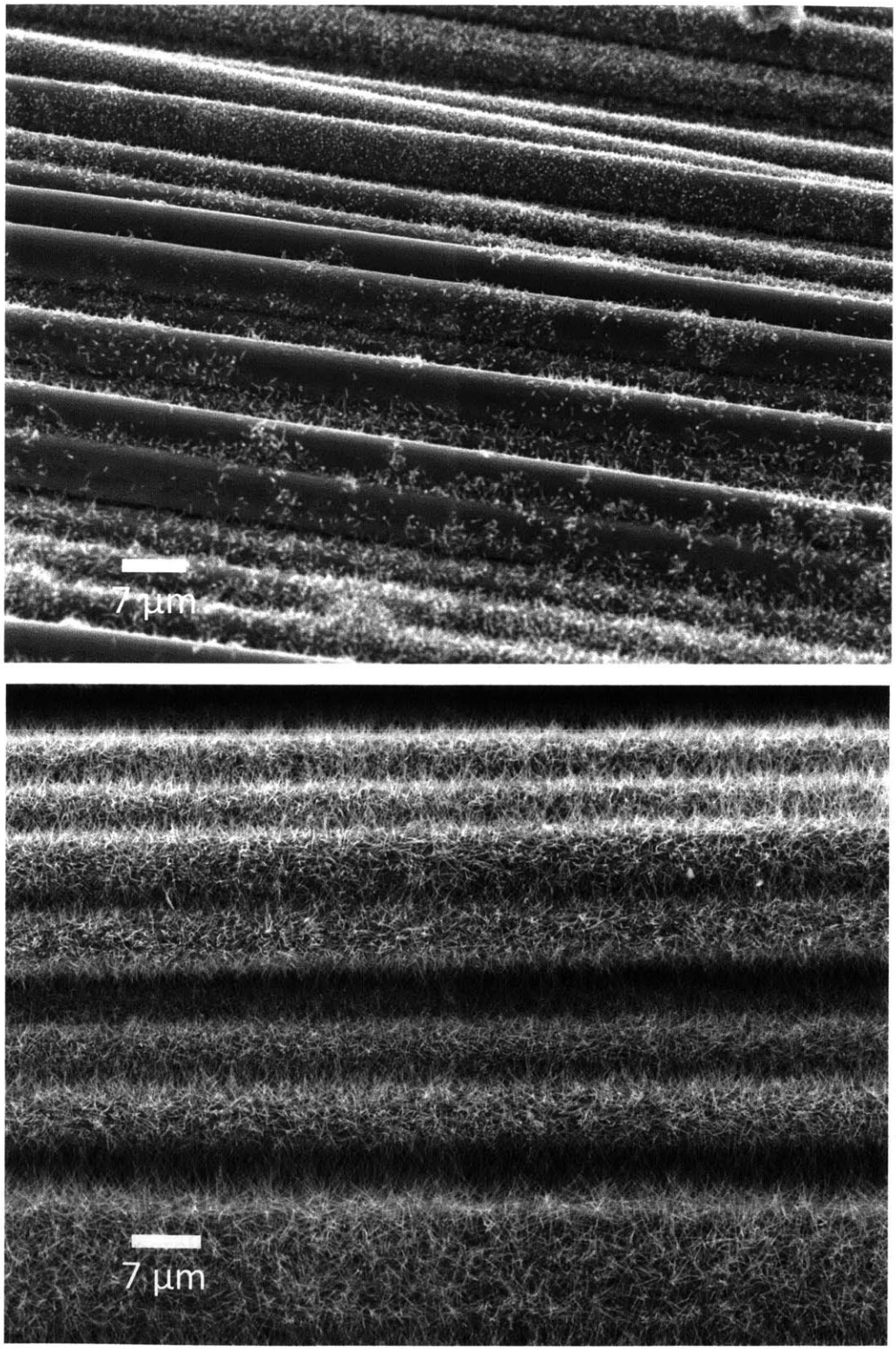

Figure 3.3 0.25wt% K-PSMA/Fe^{3+} coated fibers that had been dried in a sealed container and CVD processed *(top)*, 0.25wt% K-PSMA/Fe^{3+} coated HTR-40 fiber that had been dried in vacuum heated chamber and CVD processed *(bottom)*. Note the effect of drying conditions on CNT morphologies.

3.1.2. Selected Dip-coating Procedure

The refined dip-coating processing of unsized HTR-40 24K Tows was performed with three successive wetting cycles for the fuzzy CF in this work: Cleaning, functionalization, and catalyst deposition. First, unsized TohoTenax HTR-40 tows were extracted from a spool (kept in a desiccator) under light tension and carefully taped off at lengths ~26 cm. utilizing scotch 2600 series masking tape. The segment was then cut off from the rest of the spool, tensioned lightly by hand while water was pipetted onto the tow several times to rinse out airborne dust particulates on the fiber surfaces and facilitate handling via capillary wetting. Stainless steel weights ~ 130 g were then clamped onto one of the taped ends of the tow, while stainless steel binder clips fastened the other taped end onto a tab beneath the lid of a tall glass sealing jar (Sur La Table Nantucket Jar). This assembly allows the wet fiber tow to hang from the glass lid as shown in Figure 3.4. A vacuum port was fitted onto the side of the glass jar, and the jar was preheated in the oven to 100°C prior to insertion of the hanging tow/lid assembly into the jar. Vacuum was then pulled at a gauge pressure of -100 kPa for 5 minutes before the lid/tow assembly was removed. At this point, the tow is ready for functionalization in K-PSMA.

The tow was then unclipped from the vacuum jar lid, and submerged in a Petri-dish containing 0.25 wt. % K-PSMA solution for 5 minutes while only being held by the clamped weight and the other taped end. Upon removal from solution, a clean 20 mL scintillation jar was rolled on the surface of the tow for 3 minutes to remove excess solution, and facilitate more uniform coating application through the thickness of the tow. A drying cycle immediately ensued in which the tow was once again clipped onto the

vacuum jar lid, inserted into the preheated jar, and vacuum pulled in the oven for 5 minutes.

It was evident the coating had formed from the slight white surface tint and tow stiffening. A parafilm boat as long as the tow was formed around a wooden frame and filled with 0.05 M Fe(NO3)3·9H2O in isopropanol (IPA) catalyst solution that had been stirred for 60 minutes. Once again, the tow was submerged into the catalyst solution for 5 minutes prior to another vacuum drying cycle for 5 minutes. Finally, the clamp weight was removed from the sample, and the dip-coated tow was carefully transported to the thermal CVD furnace for CNT growth. Thus, two incipient wetness/ drying cycles was employed.

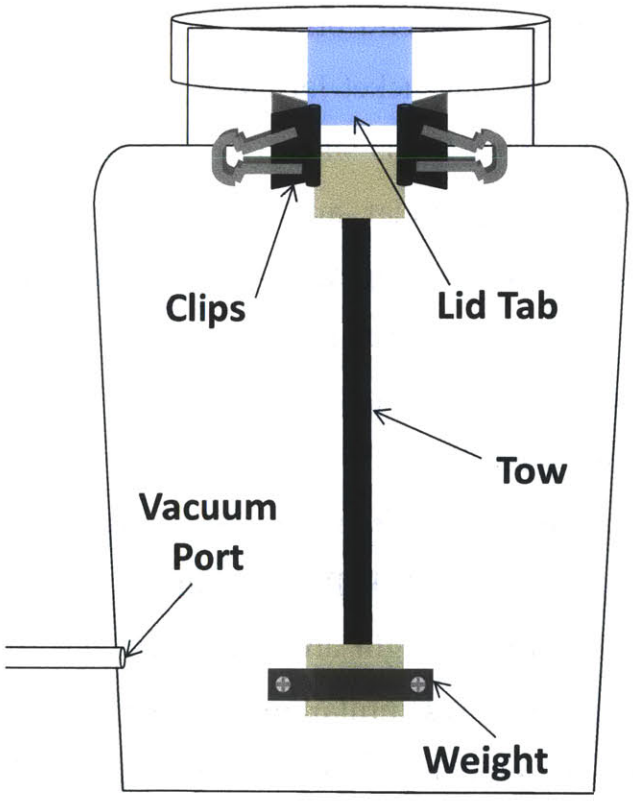

Figure 3.4 Depiction of the vacuum heating setup: A taped off tow segment hangs from a lid, lightly tensioned by a hanging weight, and inserted into the pre-heated tall glass jar. The entire assembly can then be connected to a vacuum and placed inside an oven for rapid and controlled drying of carbon fiber surfaces.

3.1.3. Growth Procedure

Since the tow stiffened from repeated coating applications, the taped portion of the tow could be safely trimmed off without ruining fiber collimation. Subsequently the tow was placed into the center of the fused quartz tube (25 mm OD, 22 mm ID, 30 cm length) and heated inside a Lindberg/Blue M Minimite furnace. The tube was first flushed with 750 sccm of Ar for 2 minutes before being subjected to H_2 and Ar flow of 400 sccm and 200 sccm respectivly. To reduce the iron catalysts on the fiber, the tube was heated to 480°C under continued H_2/Ar flow. Once the set temperature was reached, growth was initiated by turning off H_2/Ar, flowing 167 sccm of 10% C_2H_2 in Ar mixture, and flowing 17 sccm of CO_2 for 15 minutes. Finally, all gasses were turned off and flushed with 750 sccm of Ar while the furnace was allowed to cool back to room temperature.

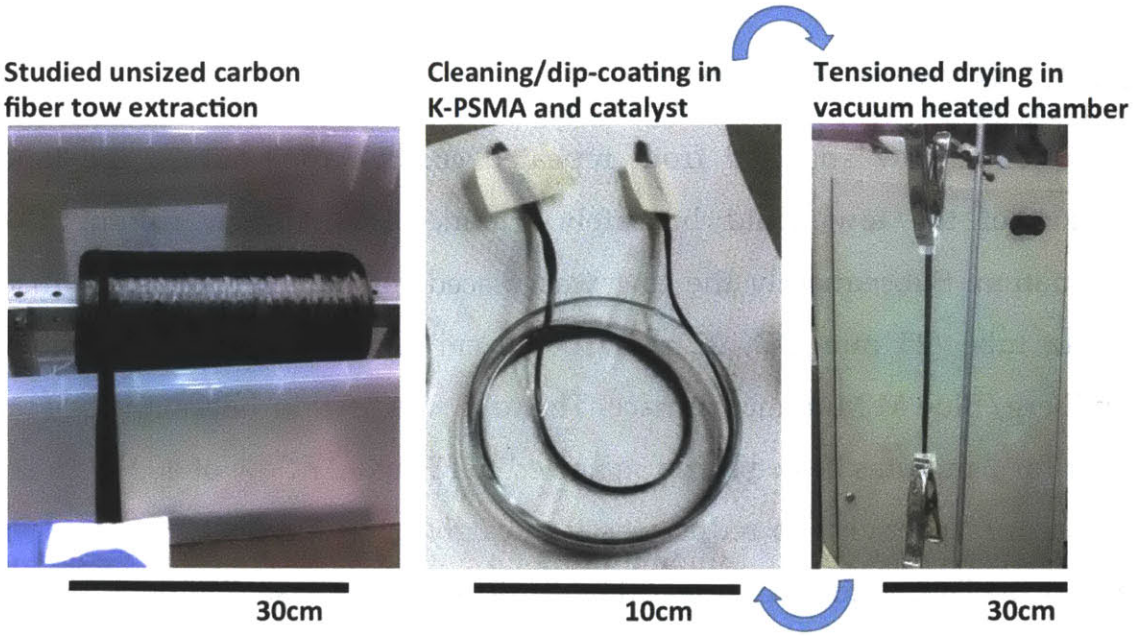

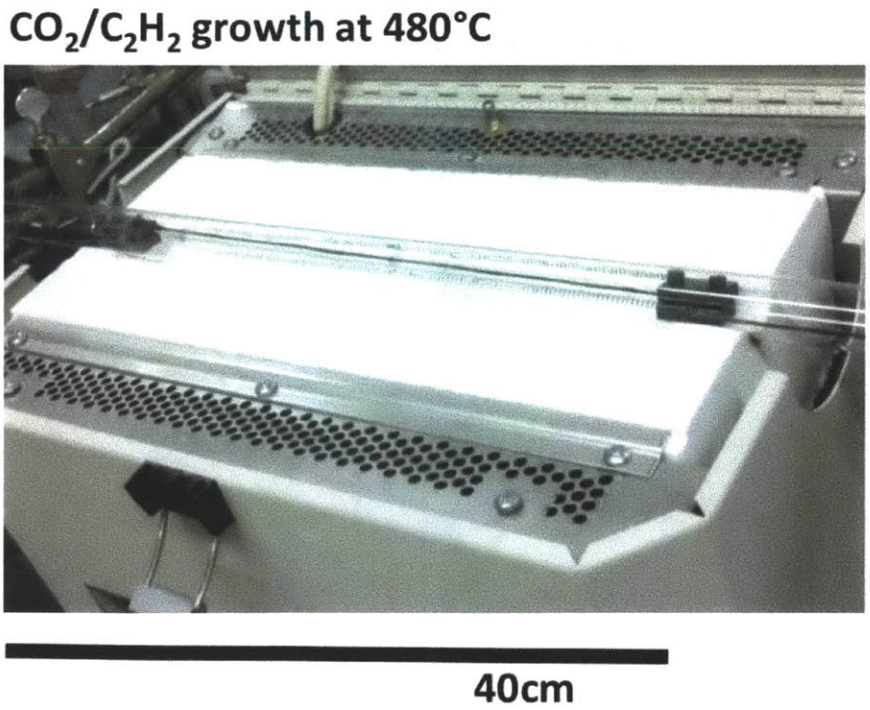

Figure 3.5 Procedure for growing CNTs on CF without degrading filament strength. Ex-PAN fibers are non-covalently functionalized in K-PSMA coating, dip-coated in iron nitrate solution, and subjected to CO_2/C_2H_2 thermal CVD at 480°C for CNT growth. Resultant tows have circumferential CNT growth around each fiber.

3.2. Unidirectional Composite Fabrication

3.2.1. Specimen Manufacturing Overview and Requirements

A unidirectional composite specimen is desired to directly assess the longitudinal tensile properties of fuzzy CFRP. Given that conformal CNT growth had been demonstrated on the unsized TohoTenax HTR-40 tows without reducing fiber tensile properties, it is advantageous to utilize the same tow for impregnation in fabricating fuzzy CFRP specimens. Additionally, this ensures that previously acquired single fiber level data can be used as direct reference for implied fiber properties within the composite. Notably, resin impregnated tows are a commonly tested unidirectional composite specimen in the carbon fiber production industry for quality control measurements of fiber tows due to low coefficient of variation between samples. Many different standards exist for these unidirectional specimens including the ISO 10618 [37], SACMA 16R-94 [38], and the ASTM D 4018 [39]. All standards stipulate similar tabbing distances (150mm) and tensile testing methodologies, however the ASTM D 4018 standard was chosen for its wide adoption in industry.

It is also generally known that the fiber volume fraction and matrix resin type affects the in-plane mechanical properties of composites [4]. Consequently, it is desireable to manufacture specimens with similar fiber volume fractions and resin systems as that used in aerospace-grade composite laminates. This allows for more direct comparison with pre-existing data points for the targeted applications of this work. A low viscosity aerospace resin infusion system Hexcel RTM 6 was selected, and a targeted fiber volume fraction of ~60% was set.

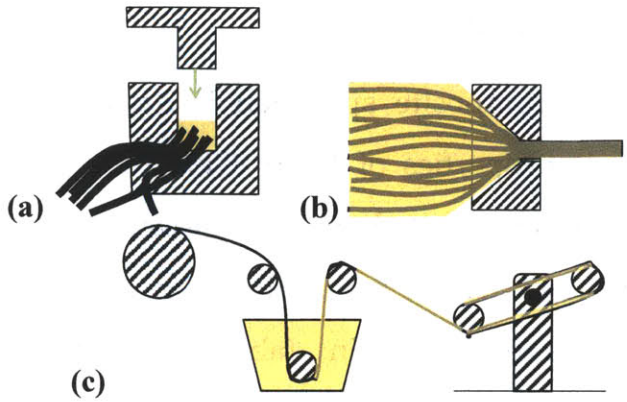

Figure 3.6 Resin Infusion Methods: Two part mold consisting of plug and groove *(a)*, wire drawing die *(b)*, resin pickup through capillary wetting *(c)*.

Multiple resin impregnation ideas were considered and attempted as illustrated above in Figure 3.6. The first trial involved inserting the dry CF tow into the groove half of a precision machined two-part Teflon mold, pipetting in RTM 6 resin (preheated to 80°C to lower viscosity) along the length of the tow, and then gently pressing the plug half into the groove. However, transverse pressure buildup on the resin during plugging resulted in resin and fiber escaping in between the sidewalls of the plug and groove such that final cured specimens resulted in a hat-shaped cross section, as well as non-uniform impregnation along the length of the tow. Another trial involved first dragging tows through resin, and then hanging in the oven for cure. These samples resulted in non-uniform sample cross-sections and resin pick-up along the length of the specimen. A similar concept commonly employed in industry is shown in Figure 3.6c in which an impregnated fiber winder rotates and pulls a CF tow into a resin bath and onto the rotating winder. The winder is then placed in an oven for curing of any polymer that had been wicked onto the fiber, and straight sections of the resultant

composite on the winder are trimmed off for tensile testing. This technique, however, necessitates precision tow spooling equipment, and subjects sample fiber volume fraction to the capillary wetting/ viscosity state of the resin and fiber surface area, which may change with the addition of radially aligned CNTs. Another technique employs dipping fibers in resin and pulling it through a wire drawing die [37] to constrain fiber and wicked resin cross section area downstream of the die. However, possible complications with this method include fibers shearing past each other locally near the bearing of the die (especially at high fiber volume fractions), and resin movement during curing cycles which may lead to resin non-uniformity through the sample.

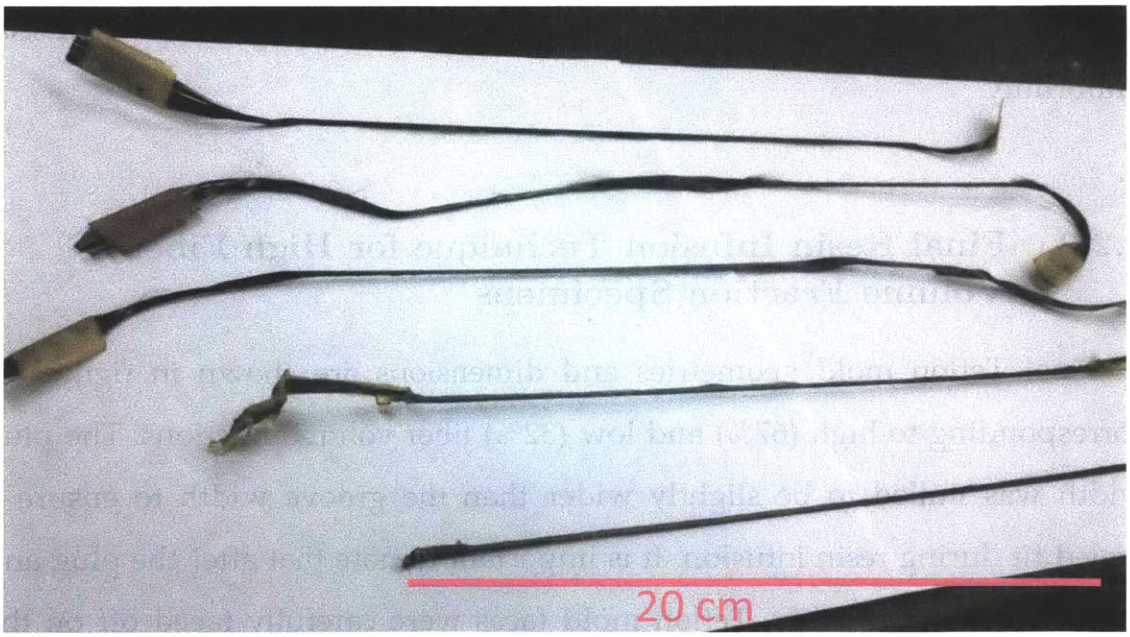

Figure 3.7 Preliminary resin impregnation trials of HTR-40 24K tow. Top sample has a hat-like cross section. Middle three specimens did not achieve full impregnation. Bottom sample was the first successful impregnation by resin infusion through a dry tow situated inside a Teflon channel.

From the aforementioned considerations and requirements to maintain the same cross sectional area for baseline and fuzzy CFRP specimens, a resin

impregnation mold that constrained final specimen geometry was a preferred option. Since the plugging of the mold halves after resin application yielded poor results, it was determined that resin must be introduced to the fibers after mold halves are combined around the dry fiber. Accordingly, after the dry tow was sandwiched inside the Teflon molds, a gravity assisted resin infusion was attempted by placing one end of the mold channel facing up into a large resin reservoir. While this result provided a very uniform sample for the first half of the specimen, the latter half was not fully impregnated, indicating that the weight of polymer was not sufficient to overcome viscous forces through the full length of the tow and channel. To increase the pressure gradient across the polymer, a vacuum assisted resin infusion method was subsequently attempted with success in achieving sample cross-sectional uniformity.

3.2.2. Final Resin Infusion Technique for High Fiber Volume Fraction Specimens

Final Teflon mold geometries and dimensions are shown in figure 3.8 corresponding to high (67%) and low (32%) fiber volume fractions. The plug width was milled to be slightly wider than the groove width to ensure a sealed fit during resin infusion. It is important to note that after the plug and groove were fit together, Teflon mold faces were carefully faced off on the four long faces to ensure groove and plug sidewalls were parallel to exterior block faces. These faces are later constrained to flat aluminum blocks to ensure the infusion channel remains straight at cure temperatures lest inherent residual stresses and anisotropy (in thermal expansion) of the Teflon block cause bowing and twisting of the infusion channel.

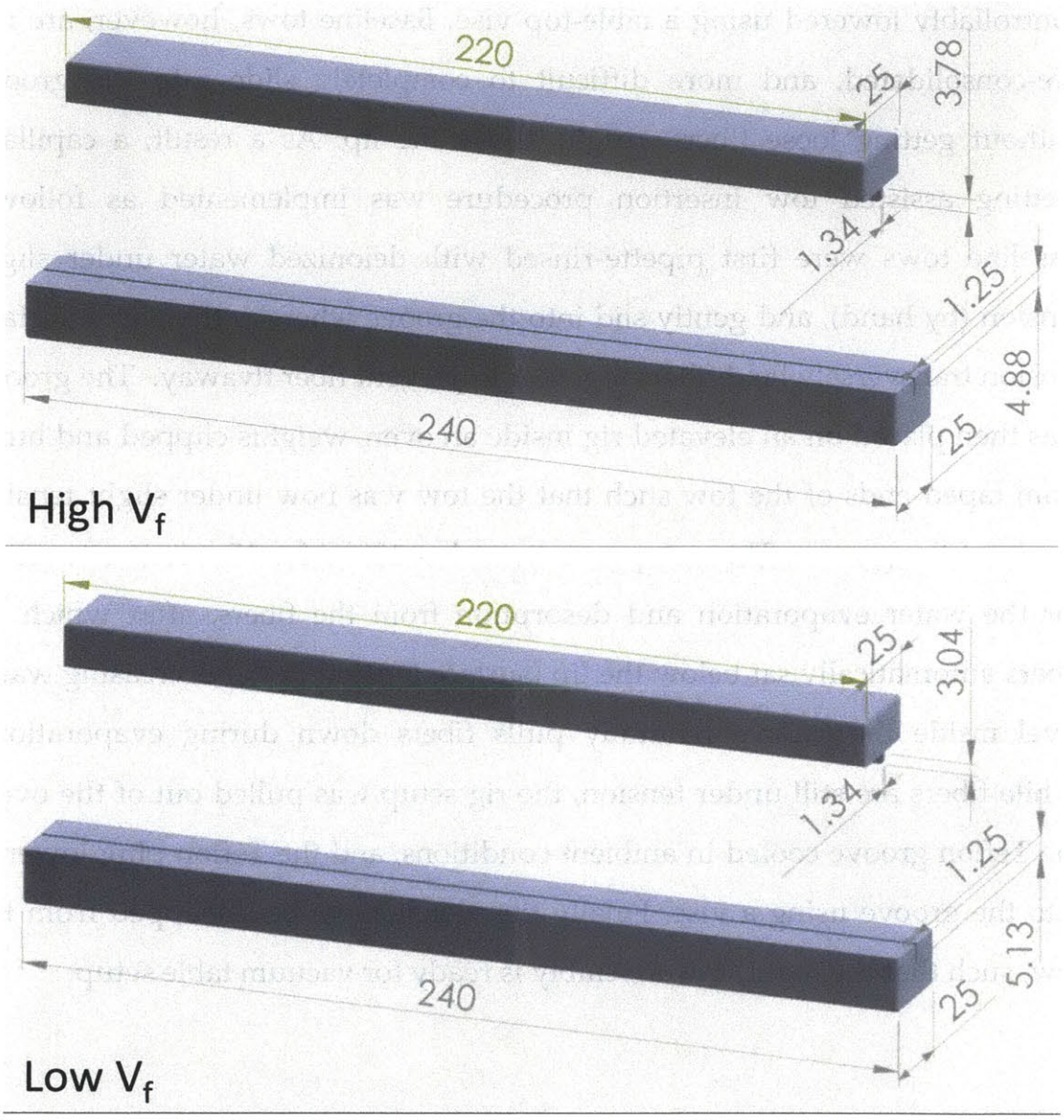

Figure 3.8 Teflon mold dimensions (in mm) for 67% fiber volume fraction specimens *(top)*, and 32% fiber volume fraction specimens *(bottom)*.

Tow insertion methods into the Teflon molds differ for baseline tows and fuzzy carbon fiber tows since the latter is stiffened and collimated *a priori* from coating applications. Fuzzy carbon fiber tows can be slid into the groove

taking care that all fibers sit below the lip of the mold with the aid of rounded laboratory spatulas. The plug is then carefully lined up with the groove and controllably lowered using a table-top vise. Baseline tows, however, are not pre-consolidated, and more difficult to completely slide into the groove without getting loose fibers caught above the lip. As a result, a capillary wetting assisted tow insertion procedure was implemented as follows: Baseline tows were first pipette-rinsed with deionized water under slight tension (by hand), and gently slid into the groove whereby the water surface tension transversely held fibers together to prevent fiber flyaway. The groove was then placed on an elevated rig inside an oven, weights clipped and hung from taped ends of the tow such that the tow was now under slight tension inside of the groove. This setup was heated at 120°C for 15 minutes to allow for the water evaporation and desorption from the fibers, after which all fibers automatically sat below the lip (surface tension of the decreasing water level inside the groove naturally pulls fibers down during evaporation). While fibers are still under tension, the rig setup was pulled out of the oven, the Teflon groove cooled in ambient conditions, and the Teflon plug lowered into the groove using a vise. Finally the weights can be unclipped from the tow, such that the mold/tow assembly is ready for vacuum table setup.

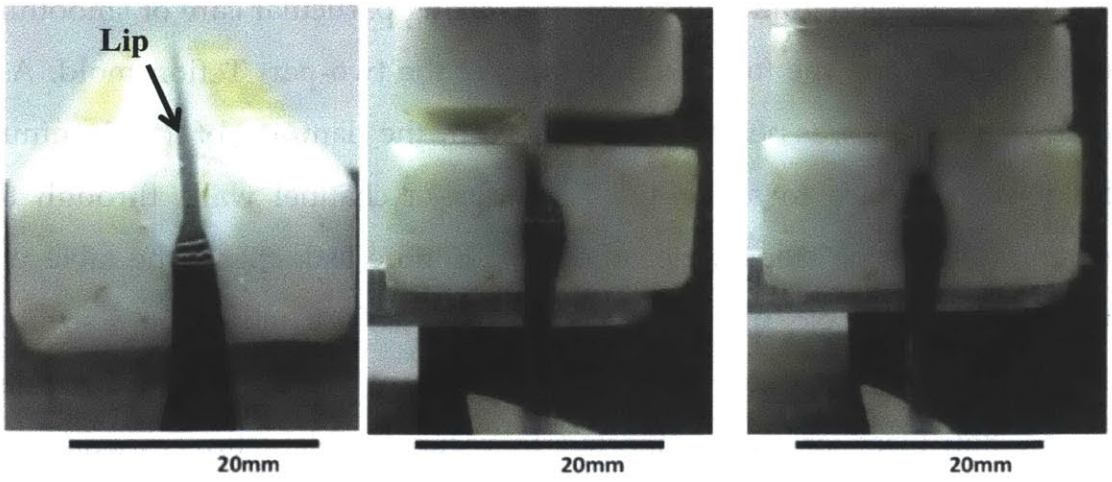

Figure 3.9 HTR-40 carbon fiber tow (baseline) is tensioned while inserted into Teflon groove *(left)*. Teflon Plug is lined up with the lip of the groove *(center)* before being slowly lowered into the groove *(right)*, thus forming a resin infusion channel.

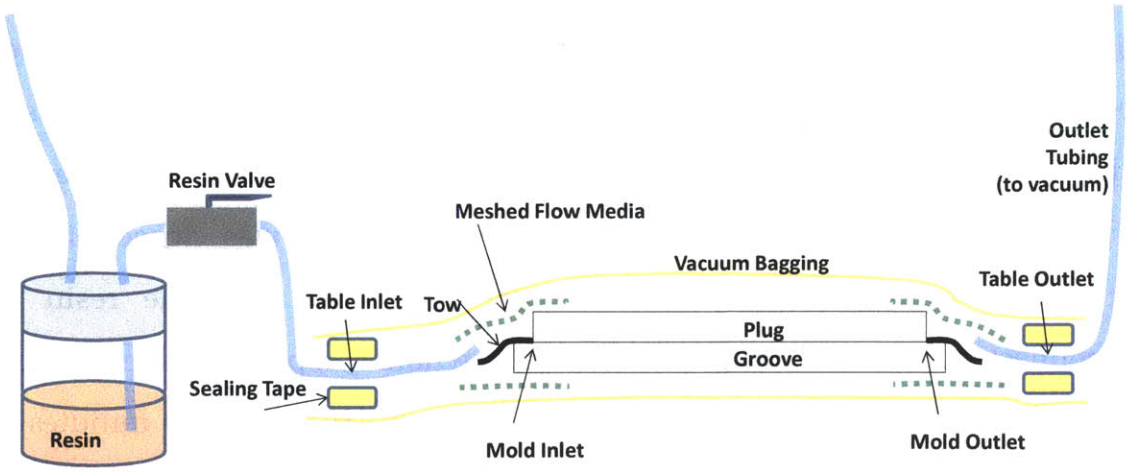

Figure 3.10 Vacuum table setup for resin infusion of high fiber volume fraction (67%) specimens. Resin front flows from left to right.

Figure 3.10 is an illustration of the vacuum table setup for manufacturing high volume fraction specimens, whereas low volume fraction manufacturing will be discussed in the next section. A thin Stretchalon 800 (1788-A) vacuum bagging was chosen for its ductility and small crease radius to limit parallel flows from resin inlet to outlet. After the bagging was sealed, the vacuum

table was evacuated gradually to -81 kPa, taking particular care of smoothing out wrinkles along the four exterior faces of the two-part Teflon mold. A 5-minute leak check was performed, followed by the clamping of flat aluminum blocks to each face to straighten the infusion channel walls through the infusion and curing steps. After another 5-minute leak check, the table was temporarily sealed off, placed inside the oven at 90°C, and then a stronger vacuum of -93 kPa applied. Meanwhile, 120 mL of premixed RTM 6 inside a 350 mL Ball glass jar was connected to vacuum table setup, evacuated to gauge pressure of -93 kPa, and heated to 90°C until bubbles ceased to surface, indicating that epoxy degassing was complete. Connection leak checks were subsequently performed on all lines and valves before the resin valve was closed and the jar vented to atmospheric pressure to create a pressure differential across the resin valve. Finally the resin valve was slowly opened to full throttle to introduce resin into the vacuum table, and left for 7 hours to allow resin to reach the outlet tubing for both fuzzy and baseline specimens.

Once the sample was fully infused, the resin valve was closed off, the outlet tubing kinked off to seal off the outlet line, and the resin jar disconnected/removed from the oven. The whole setup was subjected to a standard cure cycle of 160°C for 75 minutes, and 180°C for 120 minutes to ensure a cross-linked percentage of 94% [40]. To remove the sample, bagging was trimmed and peeled from the Teflon mold, which was then reheated to 120°C for 10 minutes to facilitate groove expansion and plug separation. Samples were lifted out of the groove from one end to the other while carefully avoiding large bending moments in the specimen. A final extracted specimen is shown in Figure 3.11. Micrometer measurements show specimen dimensions averaging 1.17 mm. X 1.18 mm with area variation of ± 4% over the specimen gauge length of 200 mm. This yields a specimen fiber volume fraction of 67%.

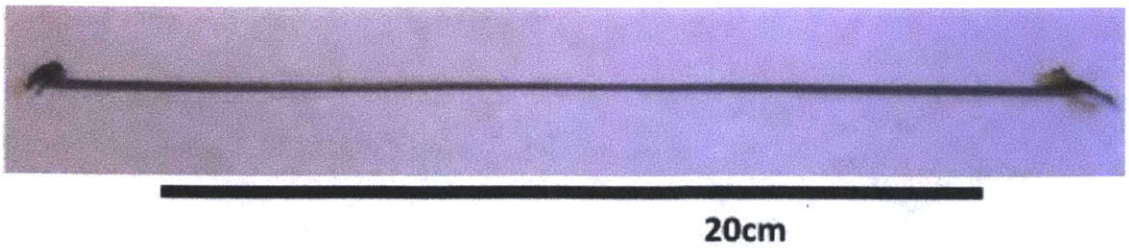

Figure 3.11 Resin impregnated tow as removed from Teflon molds

3.2.3. Final Resin Infusion of Low Fiber Volume Fraction Specimens

Leveraging the aforementioned manufacturing procedure, lower fiber volume fraction specimens were manufactured with a similar Teflon mold design and infusion table setup. However, key refinements were necessary to adapt the process to observed changes in resin flow arising from the larger channel cross-section. Initial attempts of infusing low volume fraction specimens resulted in an infusion time of only 30 minutes compared with the 7 hours necessary for 67% fiber volume fraction samples. Excessive bubbling in the outlet tubing also indicated the possibility of a leak. After cure and removal, these initial low volume fraction specimens showed easily visible voids, gouges, and pitting particularly on the surface of the specimen, thereby suggesting that air pockets were introduced and trapped within the channel. As the intended mechanical characterization includes tensile strength assessment, it is necessary to eliminate any stress concentrations such as surface defects that may initiate failure at lower loads than pristine samples. To this end, an experimental parametric study on resin infusion processing steps was conducted in an effort to minimize void formation within specimens. Key variables investigated are shown in table 4-1 and discussed below.

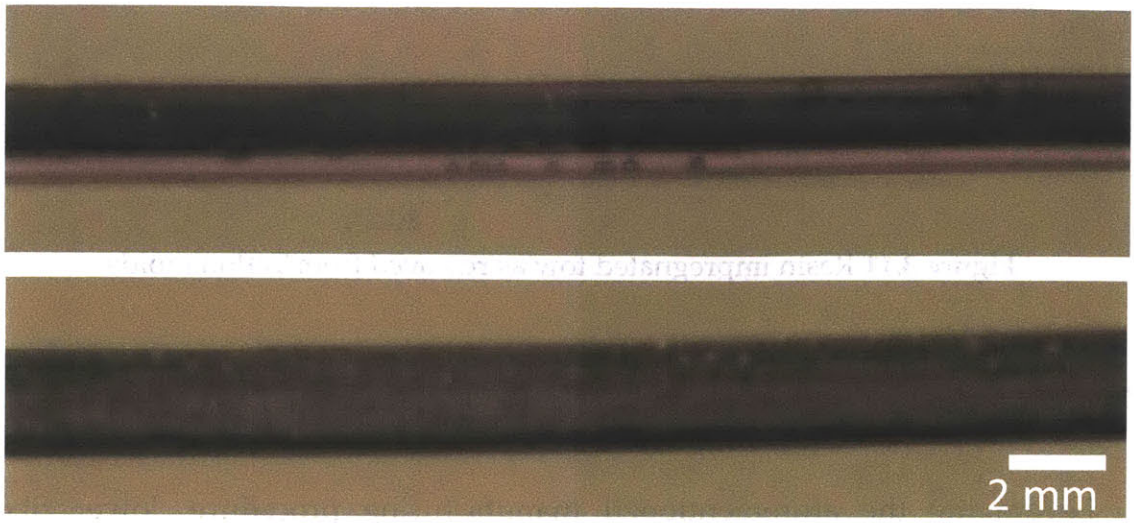

Figure 3.12 Voids *(top)* and pitting *(bottom)* are examples of observed surface defects on low fiber volume fraction specimens.

Sealing, vacuum bagging strain relief, and crease management

The defect content of initial infusion runs Fuzzy 1 and Fuzzy 2 suggest that air pockets are being introduced into the mold channel. Additionally, streams of bubbling could be found between the vacuum bagging and the exterior faces of the mold, pointing to a possible leak in the bagging setup. Hence, a double-walled sealing technique was implemented in order to provide redundancy in sealing tape adhesive failure particularly around tubing connections. Additionally, adding an additional layer of bagging between mesh sheets and outer bagging buffered undetectable punctures of the vacuum bagging. To reduce stress in the vacuum bagging in high strain areas particularly around the corners of the Teflon mold, extra folds were added as bagging strain relief. Lastly, resin flows parallel to the mold were mitigated by strategic diversion of creases so that the infusion channel served as the main conduit between vacuum table inlet and outlet.

Table 3.1 Resin infusion parametric study for 32% V_f specimens.

Sample	Vacuum Pressure (kPa)	Fiberglass Usage	Double Seal/ Double Crease	Resin Column at Mold Inlet	Vacuum Pulsing Intervals*	Externally Visible Defects	Notes
Fuzzy 1	-100	None	no	no	None	No corners or faces filled, cured resin only around the pre-packed tow	Unsealed Plug and Groove interface - parallel resin flow in mold
Fuzzy 2	-100	None	no	no	None	Top corners not completely filled, Voids in resin-rich regions, pitting on all corners	
Baseline 3	-100	3 2"x6" rolled around inlet tubing upstream of mold	no	no	5 min. kinked/unkinked for first hour	Rough corners, pitting on faces	Sample broke upon removal
Baseline 4	-100	3 2"x6" rolled around inlet tubing upstream of mold	yes	no	5 min. kinked/unkinked for first hour	Bottom corners not completely filled, Step-like bottom face	
Baseline 5	-100	3 2"x6" rolled around inlet tubing upstream of mold	yes	no	20 min kinked/unkinked. for the second hour	None	Flow front was slow despite fully open resin valve
Baseline 6	-100	3 2"x6" rolled around inlet tubing upstream of mold	yes	no	20 min kinked/unkinked. for the second hour	Pitted corners and faces at the 1/4 - 1/2 length region	
Baseline 7	-100	3 2"x6" rolled around inlet tubing upstream of mold	yes	no	20 min. kinked/unkinked for the second hour	Wavy and indented surfaces	Oven Temperature Controller Malfunction
Baseline 8	-100	None	yes	yes	20 min. kinked/unkinked for three hours after resin front reached mold outlet	Localized elongated pits	
Baseline 9	-100	None	yes	yes	10 min. kinked/unkinked for four hours	None	
Baseline 10	-100	None	yes	yes	10 min. kinked/unkinked for four hours	Localized pitting on bottom corners	
Baseline 11	-93	None	yes	yes	20 min. kinked, then 10 min. kinked/unkinked for 3.7 hrs.	Unfilled corner near inlet	
Baseline 12	-93	None	yes	yes	5 min. kinked/unkinked for first hour, 10 min. kinked/unkinked for second hour	Unfilled corner near inlet	
Baseline 13	-93	N/A	yes	no	5 min. kinked/unkinked for first hour	Aborted infusion	
Baseline 14	-85	None	yes	yes	5 min. kinked/unkinked for first two hours	Unfilled corner near inlet - more shallow than baseline 12	
Baseline 15	-85	3 2"x6" wrapped around mold inlet and outlet	yes	no	5 min. kinked/unkinked for first two hours	Pitting and voids in corners near the outlet	
Baseline 16	-85	3 2"x6" wrapped around mold inlet	yes	no	5 min. kinked/unkinked for first two hours	Pitting and voids in corners near the outlet	
Baseline 17	-85	3 2"x6" wrapped around mold inlet	yes	no	5 min. kinked/unkinked for first two hours	Pitting and voids in corners near the outlet	
Baseline 18	-85	3 2"x10" wrapped around mold inlet	yes	no	5 min. kinked/unkinked for first two hours	Elongated pit on a side face within 2 cm from outlet	
Baseline 19	-97	3 2"x10" wrapped around mold inlet	yes	no	5 min. kinked/unkinked for first two hours	None	
Baseline 20	-97	3 2"x10" wrapped around mold inlet	yes	no	5 min. kinked/unkinked for first two hours	None	
Fuzzy 21	-97	3 2"x10" wrapped around mold inlet	yes	no	No Pulsing	Large pits, unfilled corners, and voids throughout sample	Resin jar was pulled empty
Fuzzy 22	-81	3 2"x10" wrapped around mold inlet	yes	no	5 min. kinked/unkinked for first 15 min., then 10 min. kinked/ 5 min. unkinked for 1.75 hrs.	Voids at the 1/2 length in resin-rich region	
Fuzzy 23	-51	3 2"x10" wrapped around mold inlet	yes	no	60 min. kinked, then 10 min. kinked/ 5 min. unkinked for 1 hr. at flow front	Voids at the 1/2 length in resin-rich region, better than Fuzzy 22	Flow front reached mold outlet in 30 min.
Fuzzy 24	-81	5 2"x10" wrapped around mold inlet	yes	no	60 min. kinked, then 10 min. kinked/ 5 min. unkinked for 1 hr. at flow front	Voids near inlet in resin-rich region, worse than Fuzzy 22 & 23	Flow reached mold outlet in 90 min.

*5 min. kinked/unkinked refers to 5 min. kinked and then 5 min. unkinked.

Speed of resin flow front/ flow throttling

Despite the redundant sealing and vacuum bagging strain relief methods first implemented in Baseline 3, surface defects were observed for the majority of samples. Additionally, bubbling streams were still visible on the exterior mold corners, signaling that the vacuum table leak is not the primary culprit. Initial infusion trails of low volume fraction specimens already demonstrated the inverse correlation between the speed of resin flow front and the resultant quality of the part. Infusion runs for Fuzzy 1 and 2 performed with resin valve fully open required only 30 minutes for the primary flow front to reach the mold outlet compared to the 7 hours necessary for high volume fraction specimens, however specimen quality was drastically decreased. Even among multiple trials of baseline samples shown in Table 3.1, the most ideal specimen Baseline 5 simultaneously corresponded to the longest time for resin to reach the outlet. This same trend has been observed with prior work on alumina-based FFRP infusions in which faster moving flow fronts generated higher void fractions for specimens [41]. It is critical that a slower resin flow front be implemented upon the first wetting of the dry fibers. Fuzzy 21 is an example where the resin source was accidentally pulled empty, causing the infiltration of air pockets into the resin channel. A new degassed resin jar was then substituted and infused through the sample for 6 hours in an endeavor to salvage the specimen. However, the cured sample still exhibited large pitting and unfilled corners and demonstrated that initially formed voids in the channel were not advected out of the Teflon molds. Therefore, a key objective is to investigate various techniques for reducing the initial resin flow rate through the specimen.

Resin flow throttling

A primary manual method for controlling the flow leading into the sample is through the resin valve. Early in the infusion process, the valve is barely opened to create a large pressure drop and limit the flow. Gradually, as the column of resin advances through the sample and becomes subjected to larger viscous forces, the valve is opened further to enable resin to overcome flow resistance. From this method, a steady flow front can be manually maintained, and was thus implemented starting with Baseline 3. The inclusion of permeable media upstream of the infusion channel was also experimented as a method to throttle and visualize the resin flow. Baseline samples 3 through 7 included 3 layers of 2" X 6" fine fiberglass weaves that were partially rolled around the table inlet and connected to the meshed flow media. This setup limited the flow of resin downstream of the fiberglass, the efficacy of which can be observed by the pooling of resin upstream of this fabric. Indeed, the flow front velocity was drastically reduced with the inclusion of the fiberglass, but still resulted in samples with localized pitting on faces and corners. A key exception was Baseline 5 in which flow was uniquely slower -- even as the resin valve was left fully open -- and yielded a specimen with no externally detectable defects. Post-cure inspection of the table showed that only one of the fiberglass sheets overlapped the mesh flow media and may have added an additional throttle to the sample. In an effort to recreate Baseline 5's unexpected circumstance, the vacuum table was prepared almost identically in Baseline 6. Nonetheless, flow characteristics were not recreated, and sample defects were once again observed.

Elevated resin column at mold inlet

Despite flow throttling with the aid of permeable media, Baselines 3, 4, 6, 7 still exhibited pitting within the first half of the sample, but nearly ideal results in the second half. It should be considered that resin motion occurs

even during the curing cycles. As RTM 6 cross-links to form a three dimensional network, polymer density changes and creates resin shrinkage [42]. Furthermore, it has been observed that resin levels in the vacuum table outlet tubing recedes after cure. Therefore, it was hypothesized that the elevated resin column in the outlet provides a reservoir to fill in gaps during resin shrinkage and forms a cleaner specimen at the second half region. Accordingly, an elevated column of resin was also placed at the mold inlet with the goal of improving the first half of the specimen. It is important to note that the fiberglass weaves were not utilized in this case in order to permit direct flow between the resin column and the mold channel during cure cycles. Baseline 8, 9, and 10 demonstrate the result of these attempts, with a nearly defect free sample in Baseline 9. While baseline 8 and 10 were not ideal, they exhibited pitting that was localized.

Vacuum Level

To further reduce infusion velocity, vacuum levels were also tested in baseline samples 12 and 14 at -93kPa and -85kPa, respectively. While the results were not defect free, they yielded consistently localized unfilled corners near the inlet region, and pristine regions for the rest of the sample. A possible explanation may be the transient faster moving flow into the mold as the resin initially pours down the vertically oriented inlet tubing, the effect of which may be exacerbated by the absence of the fiberglass media. Therefore, aside from the observed commonality of inlet defects, no significant improvement in specimen quality could be generalized with decreased vacuum levels.

Pulsating Vacuum

Prior work has shown the efficacy of vacuum pulsing in surfacing bubbles to the flow front [43]. The cycling of vacuum levels and resin pressure allows voids to dynamically change in size and detach from surfaces such as the mold channel walls and reduce superficial defects. A simplified approach was implemented by kinking and unkinking the vacuum table outlet tubing at specified intervals. Generally, infusion times were extended with higher kinked to unkinked time ratios, resulting in a slower average resin velocity. In a few runs, higher frequency cycling was performed in order to surface bubbles in a faster moving flow front. While an in-depth characterization on this effect was not performed, it was still implemented through the final process to aid in the removal of defects.

Deflection of existing air pockets and throttling at mold inlet

Whereas the elevated resin inlet samples coupled with medium vacuum (-93 kPa) yielded consistent results, mold inlet area defects were still prevalent. In fact, observations of meshed flow media immediately exterior to the mold inlet and outlet regions revealed aggregation of air pockets through virtually all samples of this parametric study. Given that extensive measures have already been taken to create a closed vacuum table and degas resin, the origins of these bubbles are not clear in this study. Whether bubbles form through air mixing internal or external to the Teflon mold, these voids have been unavoidable and may result in sample defects if allowed to enter and remain inside the mold channels during cure. Hence, a fundamental shift in infusion strategy was considered: to deflect bubbles away from the mold inlet, and bleed out voids formed within the resin infusion channel. This concept was implemented in Baseline 15 in which 3 sheets of fine weave fiberglass 2"x 6" were wrapped around both the mold inlet and outlet. Interestingly, the aggregation of air pockets was no longer seen immediately adjacent to the

mold inlet region, but instead at the sides of the mold and the exterior of the fiberglass weaves. Additionally, the cured sample is pristine in the first half and has voids that become progressively larger towards the outlet. The setup was once again replicated in Baseline 16 and 17 in which the outlet fiberglass fabric was removed, and the vacuum level lowered. Interestingly, this method has brought great consistency in the sample quality in which all defects were only exhibited towards the mold outlet. It was hypothesized that since fiberglass layers also directly throttled resin flow into the mold channel, a larger area of fiberglass fabric parallel to the flow would provide a larger resin reservoir and facilitate the advection of bubbles in the channel past the mold outlet. With the additional pressure gradient from higher vacuum in Baseline 19 and 20, adequate resin flow had been reached such that resultant cure specimens had no externally visible defects. The time for resin to reach the mold outlet is around 3 hours, however resin flow was allowed to continue for another 3 hours to advect out defects.

Figure 3.13 Side views of specimens demonstrating the difference in fiber seating observed for low fiber volume fraction baseline specimens tows *(top)* and fuzzy CFRP *(bottom)*. Fuzzy fiber tows are pre-compacted from previous coating applications, thus resin-rich regions surround the tow.

A repeatable and satisfactory baseline impregnation technique was achieved utilizing the parameters outlined for Baseline 19 and 20.

Interestingly, these refined infusion settings for baseline samples did not function as intended for the fuzzy carbon fiber specimens. A key contributor to this difference arises from the large difference in pre-existing compaction and seating of the fiber tows. Because fuzzy carbon fiber tows are inherently stiff and consolidated from applied coatings and CNT growth, they do not evenly disperse into the full mold channel cross section as is the case for dry baseline fibers. Figure 3.13 depicts the difference in fiber seating between low volume fraction baseline and fuzzy fiber samples. Cross-sectional heterogeneity creates large gaps surrounding the tow, resulting in lead-lag behavior [44, 45], where capillary assisted wetting wicks resin faster than the slow moving macroflow, which promotes void formation in the resin-rich exterior areas of the cross section as observed in Fuzzy 22-24. Future work can be conducted to quantify the permeability of fuzzy carbon fiber tows, investigate the void formation in low volume fraction specimens, and conclusively understand the mechanisms that render high fiber volume fraction specimens robust against defect development. For the purposes of still utilizing non-ideal samples for this study, all low volume fraction composite specimens were subsequently coated with a thin layer of West Systems 105 epoxy to close external defects and reduce stress intensities. Cross-sectional heterogeneity is further discussed in chapter 4.

3.2.4. Tabbing of Specimens

The ASTM D 4018 standard stipulates that specimens can be tensile tested one of two ways: 1. Untabbed but clamped at a minimum of 25 cm. apart, and 2. Tabbed with a 15 cm. minimum gauge length. Concerns of tow crushing at testing grips and longer specimen manufacturability rendered the tabbed specimen the more attractive option. No particular tabbing material was

specified by the standard, but industrial practice typically utilizes two-part thermoset epoxy. To accurately measure material strength, it is critical to ensure the specimen fails away from the tabs. Care must be taken to enforce symmetric stress states and alignment of the specimen with the loading axis. Tabbing processes were explored and refined to fulfill these requirements.

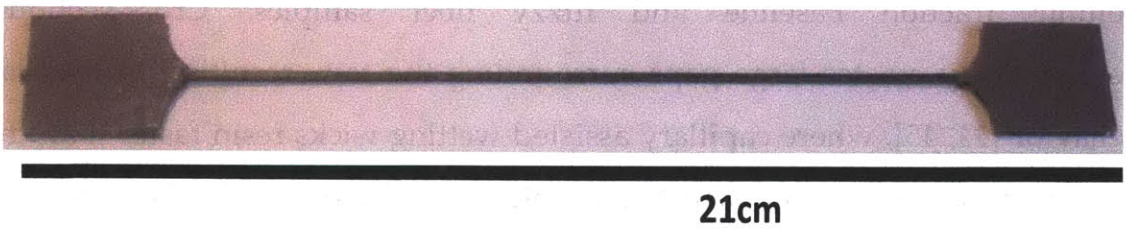

Figure 3.14 Preliminary impregnated tow specimens embedded within tapered tabs made of JB Weld Epoxy. Tabbing fracture and specimen pull-out was frequently observed with these tabs.

Preliminary impregnated tow specimens were first embedded within a Devcon 5-minute epoxy or JB weld epoxy, sandwiched between two laser-cut sandpaper strips as shown in figure 3.14. However, tensile testing of these samples resulted in pull out below 1kN, and frequent tab fracture. The process was refined by changing tabbing geometry, reinforcing tabbing material with fiberglass inserts (for load sharing), and incorporating a higher strength epoxy (Henkel EA). The final successful tabbing procedure is as follows: Bonding interfaces of impregnated tow specimens were lightly prepared with 220 grit sandpaper and sequentially cleaned in solutions of acetone, methanol, isopropanol, and deionized water such that residues of the previous solvent were dissolved. A set of aluminum tabbing molds (Figure 3.15) were spray-coated with 3 layers of Freekote mold-release agent. The rough faces of laser-cut 220-grit sandpaper pieces were then adhered to the

face of the mold using 3M Super 77™ adhesive spray, and the smooth faces coated with a 2 mm thick layer of Henkel EA. Once the impregnated tow specimen was placed on the guide of one mold half, both mold halves could be placed together. Fiberglass inserts were transversely squeezed into the epoxy until they contacted the specimen (wiping off any excess epoxy), and mold halves were taped together with flash tape before being cured in the oven at 100°C for 1 hour. After cool down, tabs can be carefully debonded from the molds using straight-edge razors dipped in isopropanol. Excess 3M Super 77™ adhesive was removed with isopropanol, and the tabs were trimmed with a bandsaw.

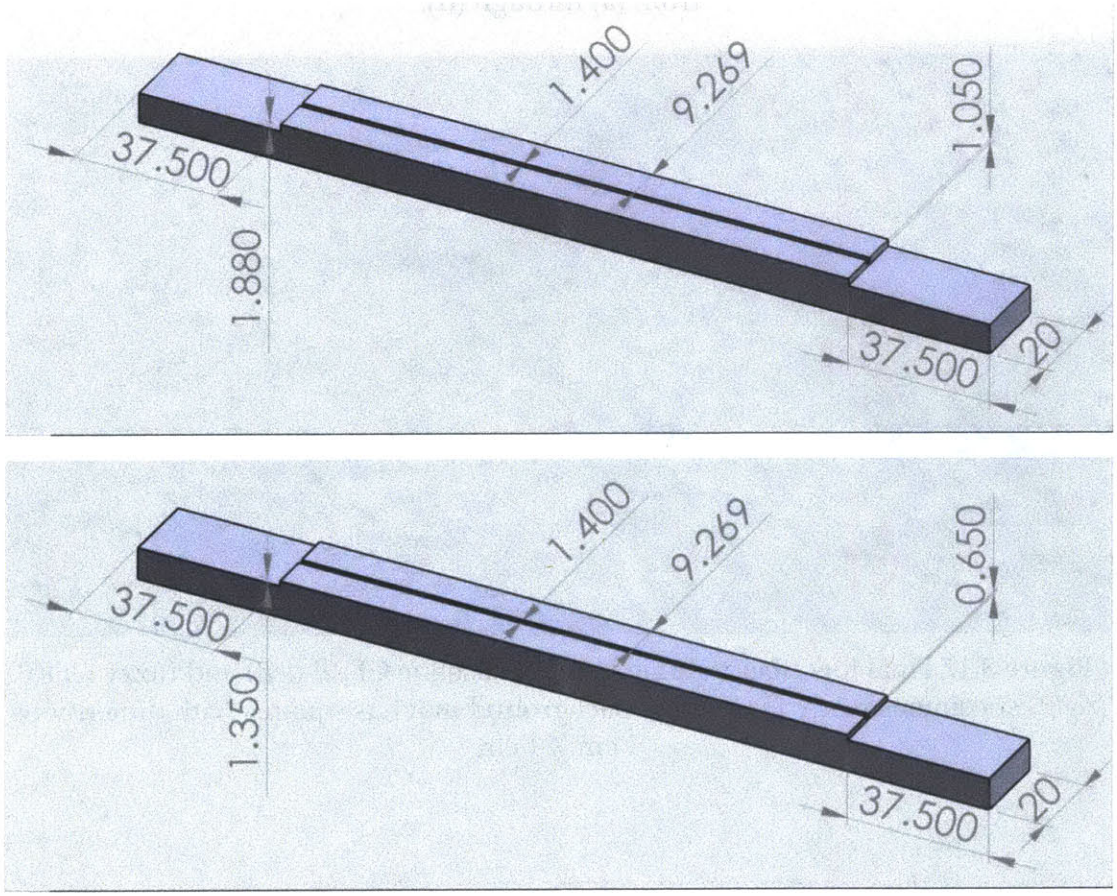

Figure 3.15 Aluminum tabbing mold dimensions (in mm) for 67% fiber volume fraction specimens *(top)*, and 32% fiber volume fraction specimens *(bottom)*.

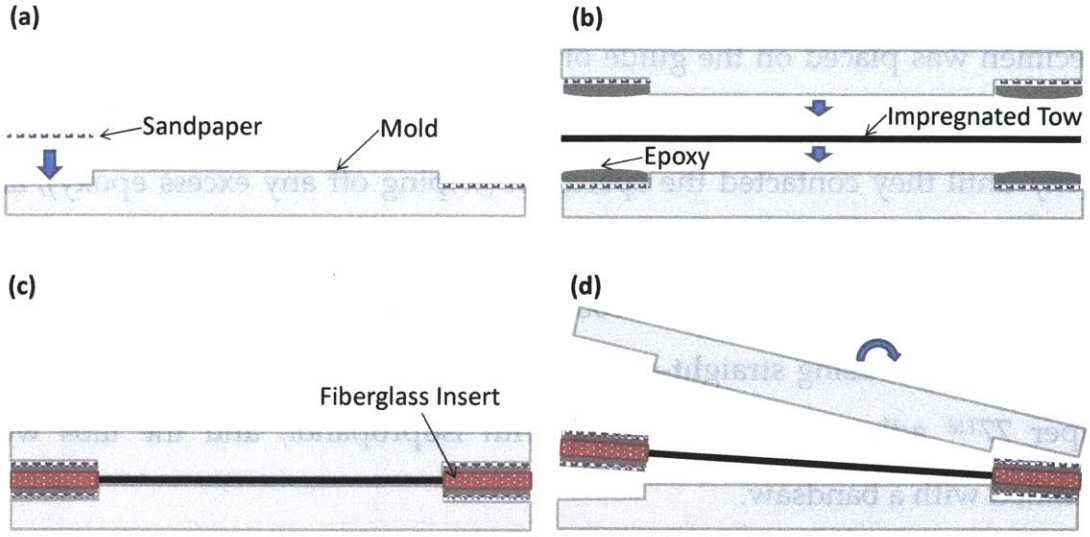

Figure 3.16 Impregnated tows were tabbed on molds utilizing the steps shown from (a) through (d).

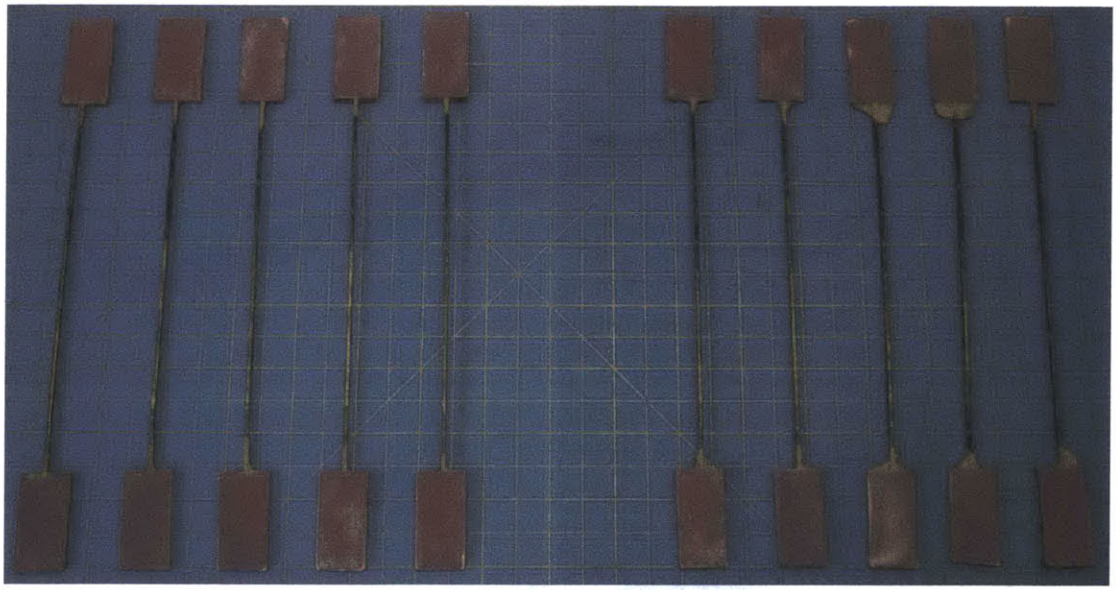

Figure 3.17 Final low fiber volume fraction baseline CFRP *(left)* and fuzzy CFRP *(right)* specimens ready for testing. Background mat has squares with dimensions 1 cm X 1 cm

3.3. Testing

3.3.1. Speckling and Strain Measurements

Whereas mechanical extensometers and strain gauges are often used for measuring local longitudinal elongations of composite specimens, optical strain mapping technique was deemed more appropriate for thin resin impregnated tow specimens that are under study. Preliminary trials with the Epsilon 3442 extensometer were met with mounting challenges due to the small area of these specimens. To counter surface slippage, arms were clipped tighter around specimens. This however, caused extensometers blade tipped arms to dig into the material, rendering it a concern for introducing surface damage for these 1.15 mm thick specimens.

If material displacements are properly tracked with a high resolution camera, digital image correlation (DIC) techniques will allow for tracking of a multitude of points, higher spatial resolution, and strain measurements averaged over (relatively larger) areas of interest. In addition, as a non-contact method, DIC can measure specimen strains up until failure without incurring damage to the sample or an extensometer - the latter concern generally requires pausing the tensile test to carefully unclip the extensometer prior to straining to failure.

In this study, specimen faces were first painted with a layer of white base paint before being speckled with black ink through a medium airbrush. This speckling method achieved a much sharper contrast than a direct application of white speckles on the specimen surface. Samples were then mounted inside the testing machine, and a voltage regulated lightbox (to avoid flickering) positioned to illuminate the center of the specimen. A one-CCD PointGrey Grasshopper camera with a Navitar Zoom 6000 telephoto lens was placed 1 meter from the testing plane. By measuring the grip rotation angle

(relative to the load frame) and marking out a radius normal to the testing plane, care was taken to ensure the camera's line of sight was normal to the specimen face to prevent any perspective skew and out-of-focus regions. To prevent specimen blurring, the lightbox was dialed full, and the camera exposure time reduced until images were just below oversaturation. Additionally, a critical parameter for tracking accuracy is speckle size. Speckles too fine may encounter aliasing issues in which errors are made in delineating the boundaries of speckles. Generally, speckles that span more than 5 pixels was found to be conducive towards accurate displacement tracking.

A specialized image acquisition software VicSnap™ by Correlated Solutions was utilized to interface with the optical camera, capture images, and synchronize it with analog data every 250 ms. After testing, recorded speckle images and synced load/crosshead displacement values were imported into the Vic2D software. An area of interest can be selected on images, within which displacement gradients could be calculated, averaged, and exported with load data to generate a stress-strain plot. This setup has been previously tested on smaller speckled area polymer nano-composite (PNC) specimens [46], and been shown to yield strain values that agree with other calibrated strain measurement setups.

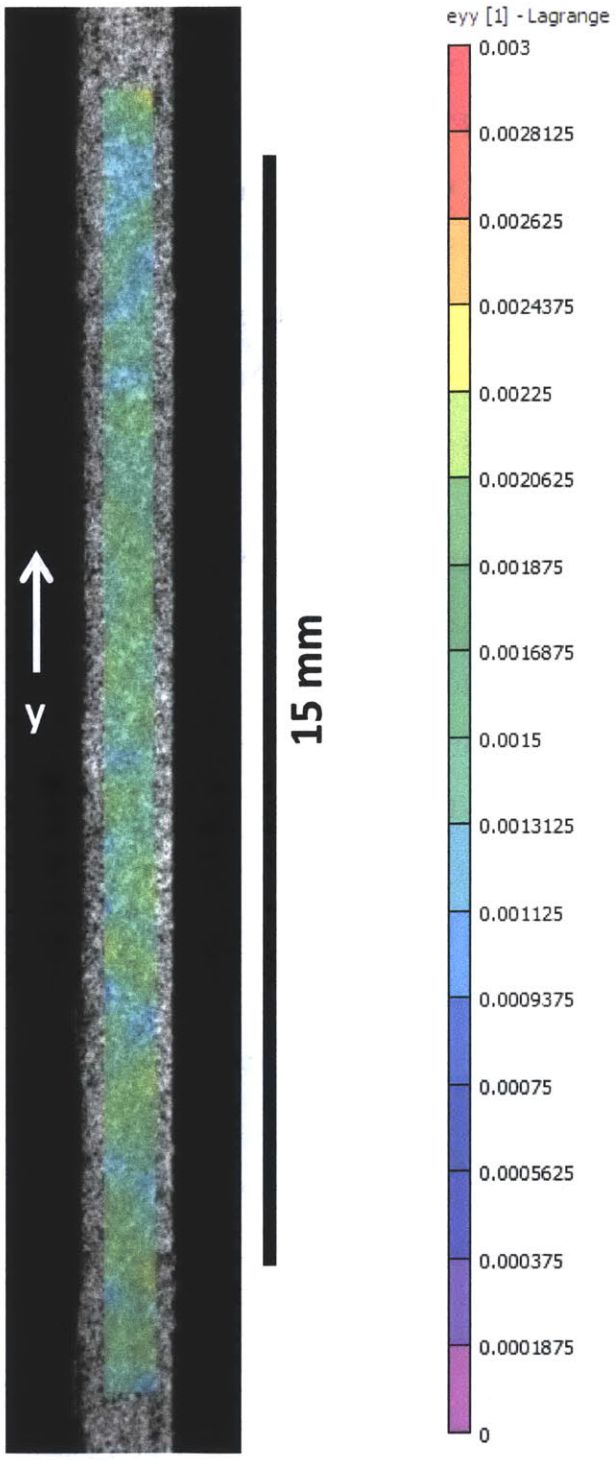

Figure 3.18 An example of longitudinal (ε_{yy}) strain values calculated for a speckled specimen using the Correlated Solutions Vic2D software. The colored rectangle over specimen denotes the area over which displacement gradients were calculated.

3.3.2. Testing Machine Setup

Load measurements were acquired by a 220 kN capacity load cell within an Instron 1332 load frame. Pneumatic action grips enabled gripping pressure to be set to 2.1MPa, which was critical in preventing specimen pull-out as established in preliminary testing. In order to ensure a symmetric and uniaxial stress state in the center of the specimen, specimens were also aligned with the loading axis by bringing the crossheads together and marking the central meeting points. Guides were adhered to each mark, and specimens were placed along the guides during clamping of the grips. Testing was conducted at a quasi-static strain rate of 1mm/min until specimen failure in accordance with the ASTM D 4018 Standard. Load and crosshead displacement analog waveforms were input to the computer via a data acquisition board, and captured at 250 ms intervals within the VicSnap software. Videos of lower Vf fuzzy CFRP samples during testing were also acquired by a separate Point Grey Grasshopper camera recording at 200 fps. This frame rate however, is too low for capturing initial point of specimen fracture.

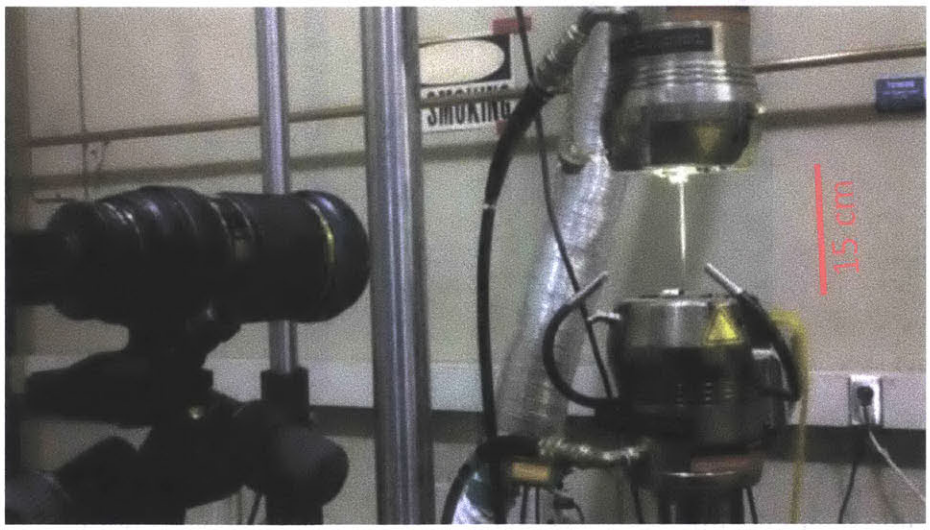

Figure 3.19 Testing setup of a clamped specimen inside the Instron with strain measurements performed through optical strain mapping.

Chapter 4

Results

4.1. High Fiber Volume Fraction Specimens

The ASTM D 4018 standard specifies a minimum of four successful tests per treatment as a sufficient sample size for accurately characterizing tensile strength and modulus. A test is only accepted if fracture occurs within the gauge length of the specimen away from the tabs. Any failure at the grips/tabs such as specimen pull-out or fracture is eliminated from consideration since it is not representative of material strength under uniaxial stress state. Generally, all specimens were observed to fail catastrophically given the high strain energy stored within the brittle carbon fibers. Examples of specimens after fracture is are shown below in Figure 4.1, where the case on the right is more typically observed.

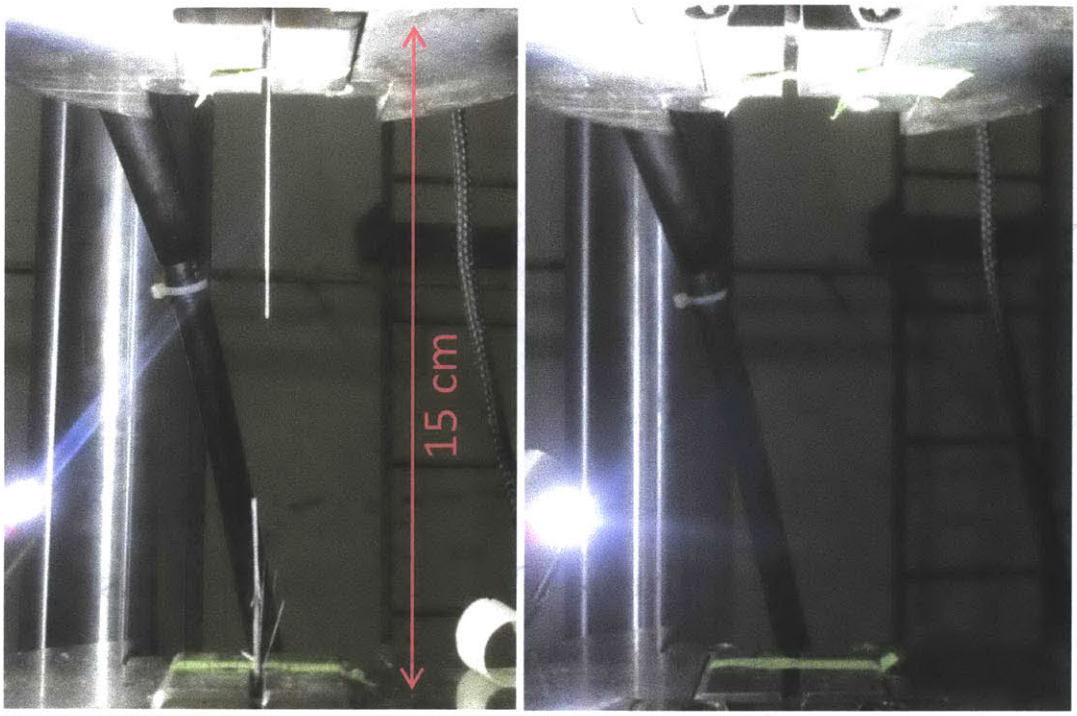

Figure 4.1 Impregnated tow specimens after dynamic failures in simple tension. A few cases have specimens remaining by the tabs (left), while most have virtually no material remaining (right).

Whereas *post-mortem* inspection and SEM imaging of the remaining fracture surfaces were performed for some specimens, results are not indicative of the original fracture mechanism. Stress waves from the first points of fracture propagate and reflect off the clamped ends to initiate secondary fractures and shattering of the specimen, rendering it difficult to identify the primary failure. As a result, all final tested data points were included, and may result in a slight downward skew for strength averages. Experimental refinements can be performed in the future with the aid of high-speed cameras in order to capture initial fracture sites, identify outlying data points, and understand the typical modes of specimen failure.

A typical stress strain plot is shown below (Figure 4.2) for a baseline CFRP high fiber volume fraction specimen. Noise levels of strain measurements are low and the strain at failure is well within range predicted using the as-

received HTR-40 fibers. Additionally, the fiber-dominated tangent modulus of the specimen rises with increasing strain, similar to that observed for a single filament test of HTR-40. This phenomenon is expected since the core of PAN-based carbon fibers comprises an interwoven ribbon network of turbostratic graphite crystallites that straighten with increasing tensile strain [29].

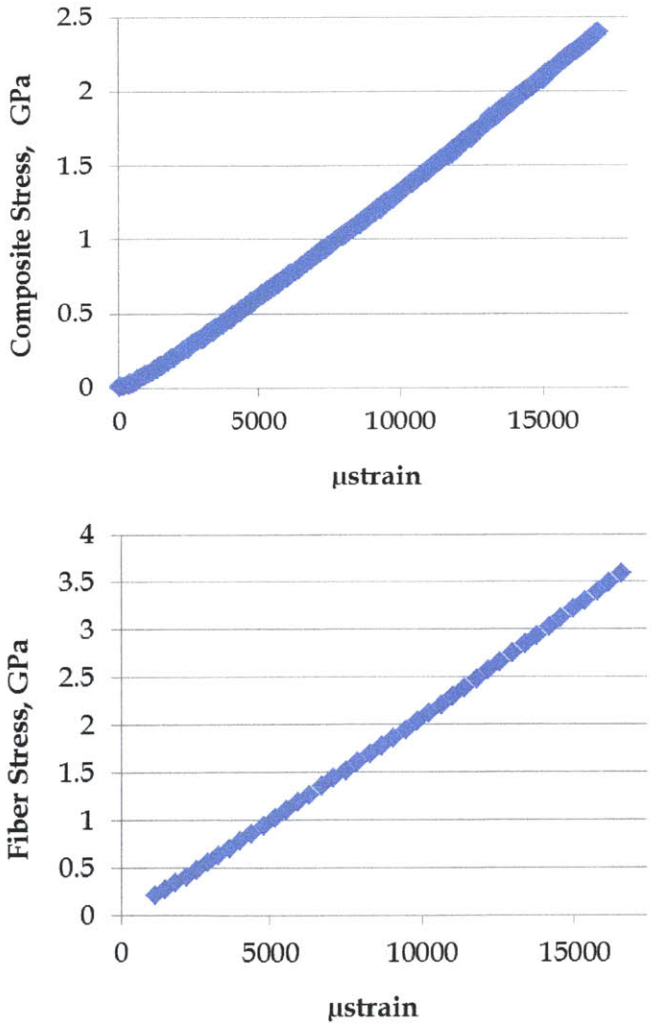

Figure 4.2 Typical stress-strain curves for 67% Vf HTR-40 baseline CFRP under tensile testing *(above)*, and for single HTR-40 baseline fibers as received *(bottom)*. Note the small initial gap in single fiber data due to corrections for delayed triggering of extension recording.

Composite stress values were calculated by dividing breaking load by the initial cross sectional area of the composite. As stipulated by the ASTM standard, chord modulus E_c values were taken between the strain limits of 1000-6000 μstrain, where consistently elastic behavior can be observed. Plotted modulus values are shown in Figure 4.3 using Equation 4.1. See Appendix A for tabulated numerical values.

$$E_c = \frac{(P_{upper} - P_{lower})}{A_c \cdot (\varepsilon_{upper} - \varepsilon_{lower})} \tag{4.1}$$

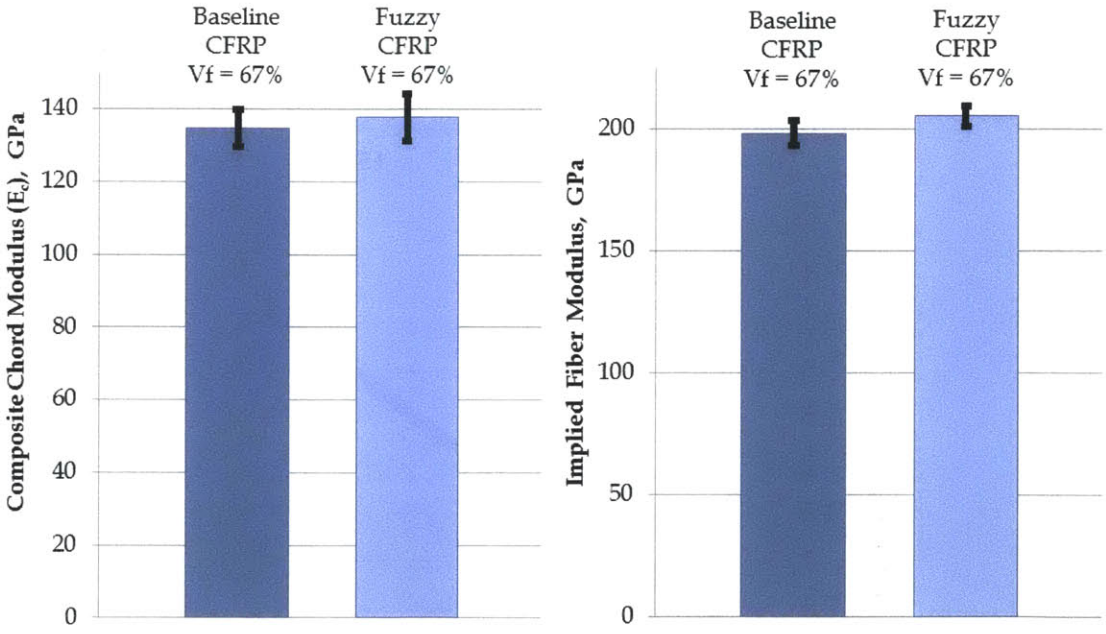

Figure 4.3 High fiber volume fraction chord composite modulus (left) and implied fiber modulus (right) taken between 1000 and 6000 μstrain.

Composite modulus values align with micromechanical predictions. Longitudinal modulus values can be estimated by assuming a representative volume element of slender fibers perfectly bonded to and strained in parallel

with polymer matrix (iso-strain conditions). From equilibrium of the element and constitutive relations (of the polymer, fiber, and composite), a rule of mixtures (ROM) expression can be developed for the composite longitudinal modulus in Equation 4.2 [4]:

$$E_{c\_ROM} = E_f V_f + E_m(1 - V_f) \tag{4.2}$$

Since it is of interest to derive a chord modulus value comparable to experimental data, baseline unsized HTR-40 single filament testing data previously acquired [33] was reexamined to calculate an average fiber chord modulus value of 204 GPa between 1000 and 6000 microstrain. Matrix modulus of 2.89 GPa was taken from the Hexcel RTM 6 data sheet [40]. Utilizing these input values, a 67% V_f unidirectional baseline composite should have a chord modulus of 137 GPa, which is in close agreement with experimental data.

Similarly, a multi-scale ROM can be utilized to estimate the fuzzy fiber longitudinal chord modulus, where matrix regions immediately adjacent to fibers are treated as aligned polymer nanocomposites (A-PNCs) with radially aligned CNTs [47]. If the assumption is made that 1-micron-tall CNTs are perfectly aligned and normal to CF surfaces in fuzzy CFRP, then longitudinal modulus of the matrix could be estimated as the transverse modulus of an A-PNC, which is approximately the same as that of neat epoxy [48]. Thus fuzzy CFRP longitudinal modulus values would be expected to be the same as that of CFRP. Even if the alignment assumptions were relaxed to account for wavy and/or un-aligned tube morphologies observed in SEM images of fuzzy carbon fibers, the CNT volume fractions are low enough (less than 1%) in the polymer that matrix longitudinal modulus values would remain virtually unchanged. Therefore, as anticipated with the above considerations, the fuzzy

CFRP composite modulus was experimentally observed to be the same as that of CFRP.

Since the majority of composite load is carried through the stiff reinforcing fiber, it is often desired to infer fiber properties by assuming a negligible uniaxial load bearing contribution of the polymer matrix. Implied fiber modulus values can be calculated in accordance with ASTM D 4018, where the ROM equation 4.2 is rearranged to solve for E_f assuming that the matrix terms vanish. These values allow for direct comparison of fiber performance within the context of a composite, and are consequently used within the fiber production industry. As expected from prior single filament results [2], Figure 4.3 demonstrates that implied fiber modulus of fuzzy carbon fibers are preserved.

$$E_{f\_Implied} = \frac{E_c}{V_f} = \frac{\left(P_{upper} - P_{lower}\right)}{n \cdot \pi \cdot r_f^2 \left(\varepsilon_{upper} - \varepsilon_{lower}\right)} \tag{4.3}$$

Of particular interest is the tensile strength comparison, shown in Figure 4.4. Composite breaking strengths were calculated by dividing breaking load by the initial cross-sectional area of the composite specimen.

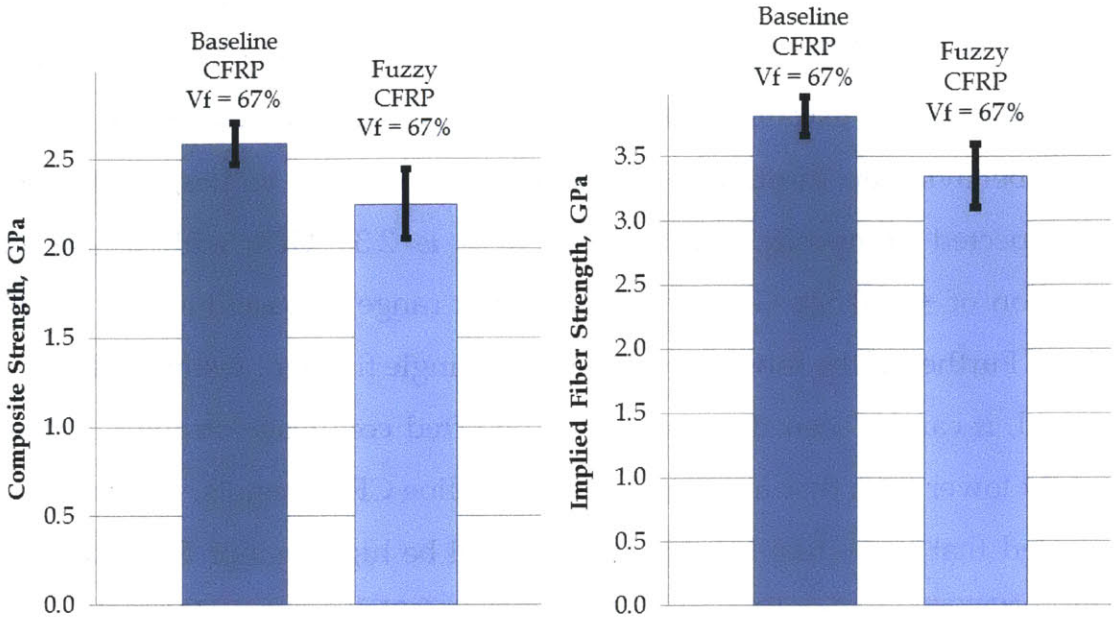

Figure 4.4 High fiber volume fraction composite tensile strengths (left) and implied tensile strengths (right). A 12% loss in implied fiber tensile strength is observed for 67% Vf fuzzy CFRP specimens, which is likely due to high transverse compression in Teflon molds.

Once again, a micromechanical prediction of composite strengths can be generated and compared with experimental values. Similar representative volume elements, iso-strain assumptions, and linear elasticity were held. However, an additional assumption is that the failure of the composite occurs at the fiber's strain-to-failure, which is close to what has been observed experimentally in Figure 4.2. After applying force balance at breaking strain, a ROM relation can be developed again for composite strength [4] as given in Equation 4.4.

$$\begin{aligned} \sigma_{c_{max_{ROM}}} &= \sigma_{f_{max}} V_f + (\sigma_m)_{\epsilon_{f\,max}} (1 - V_f) \\ &\approx \sigma_{f_{max}} V_f + E_m \epsilon_{f_{max}} (1 - V_f) \end{aligned} \tag{4.4}$$

Previous single filament testing of HTR-40 fibers yielded dry fiber strengths of 3.46 GPa with a standard deviation of 0.786 GPa and breaking strain of ~ 17,000 μstrain. $(\sigma_m)_{\varepsilon f}$ can also be estimated by assuming a linear elastic behavior up through fiber break. Inserting these values, we find that the expected composite breaking strength is 2.33 GPa with a standard deviation of +/- 0.526 GPa, which is within range of baseline experimental values. Further, if the inherent variability of single filament testing values was ignored, it can be seen that the mean predicted composite strength value is slightly lower than that measured in the baseline CFRP results. However, it is expected that the actual breaking values will be higher since ROM does not capture the matrix load transfer ability around fiber rupture [4] and the fact that a gauge length dependence exists for single brittle fiber testing derived strengths [49]. As another way of seeing this effect, implied fiber strengths can be calculated and then compared to the single fiber tested strengths through equation 4.5.

$$\sigma_{f\,Implied} = \frac{\sigma_c}{V_f} = \frac{P_{max}}{n \cdot \pi \cdot r_f^2} \tag{4.5}$$

Indeed, the implied fiber strength of 3.81 GPa was observed to be 10% higher than the single fiber testing derived mean (3.46 GPa) due to the matrix "bandaging effects" around fiber breaks and defects. A comparison of high volume fraction baseline and fuzzy CFRP samples reveals a statistically significant drop of -12% in mean tensile strengths of fuzzy carbon fibers. This finding was unexpected since single filament testing previously demonstrated that fuzzy HTR-40 fibers have preserved tensile strengths. In order to identify the origins of this strength loss, two possible explanations were hypothesized beyond CNT growth damaging the CF. As circumferential CNT growth on

CFs have been shown to alter fiber/matrix interfacial shear strengths [3], perhaps interface properties may have been modified, driving different composite failures and influencing toughness to pre-existing defects in the specimen . A second hypothesis was that fuzzy carbon fibers were damaged during specimen manufacturing, necessitating a re-examination of processing steps. After reviewing all steps, one fabrication process required further inspection: insertion and compaction of fuzzy fibers within the Teflon molds to a fiber volume fraction of 67%.

Considerations of fiber packing within the Teflon mold channel indicate the likelihood of transverse stress being imparted onto fuzzy carbon fibers. When cylindrical fibers are constrained to a fixed volume, a hexagonal array would yield the highest packing efficiency and maximize inter-fiber distances to prevent fiber-fiber contact that might create surface damage. However, in typical composite manufacturing, fibers do not spread apart uniformly to form uniform gaps between fibers. In fact, a practical processing limit of ~70% fiber volume fraction is often encountered before fiber damage is observed [50, 51]. This limit is also lower than a square packed array scenario, which can yield a maximum volume fraction of 78% if fibers are in contact with each other.

Even if it is assumed that 7-micron-diameter HTR-40 fibers manage to disperse evenly into a square array, a 67% fiber volume fraction results in an inter-fiber distance of 0.5 microns, which is already shorter than CNT lengths (~1 micron) typically observed in fuzzy carbon fibers. Realistically, because composite fibers do not pack as regularly as square arrays and CNT arrays are not observed to inter-digitate, transverse stresses and surface contact will arise from compressing fuzzy fibers to a high carbon fiber volume fraction of 67%.

The potential for fiber damage is further exacerbated by the handling quality of dry fuzzy carbon fiber tows, which are pre-consolidated by residual coatings and CNT layers. The presence of more inter-fiber material and stiffer connections between adjacent fibers imparts greater transverse stresses and friction before fiber mobilization into the rest of the mold channel cross-section is achieved. Consequently, there is no reason to suspect that fuzzy carbon fiber tows (especially their surfaces) could be damaged during mold compression. To rigorously eliminate the possibility of compromised filaments, a study testing impregnated tows subjected to virtually no transverse compression was necessary. Leveraging the existing manufacturing techniques of high volume fraction specimens, new specimens with larger cross-sectional area and low fiber volume fractions were fabricated.

4.2. Low Fiber Volume Fraction Specimens

The key motivation of the low fiber volume fraction study is to eliminate manufacturing induced damage in order to measure inherent tensile performance of unidirectional fuzzy CFRP. To this end, both baseline and fuzzy carbon fiber tows were inserted into a resin infusion channel with a taller cross-section such that filaments were not transversely compressed. In order to choose the appropriate specimen dimensions, an appropriate fiber volume fraction target was first established.

Considerations were made about the packing scenarios of fuzzy carbon fibers that would ensure no compression. If fuzzy carbon fibers were assumed to have an effective diameter of 9 microns (7-micron-diameter carbon fiber with 1-micron-tall radial CNT), then a hexagonal close packed

(HCP) scenario of these effective fibers would portray the highest packing density where only the tips of CNTs touch. In this idealized situation, the actual carbon fiber volume fraction is 55% - further suggesting that 67% fuzzy fiber volume fraction specimens were compressed beyond the threshold to damage them. Once again, in practice, it is erroneous to assume effective fibers will spread evenly to achieve the HCP configuration. Thus, the 55% Vf is only a theoretical upper bound for the targeted carbon fiber volume fraction. If the less spatially efficient square packing is instead considered for the effective fibers, then the maximum carbon fiber volume fraction now becomes 47.5%. Yet again, square packing is an idealized depiction of actual fiber dispersion, and as such, targeted carbon fiber volume fraction should be lower than 47.5%. In narrowing the operable window, the chosen Vf must be greater than critical $V_{f\_min} = (\sigma_{m\_max} - (\sigma_m)_{\varepsilon fmax})/(\sigma_{m\_max} - (\sigma_m)\varepsilon_{fmax})) = \sim 1\%$, which defines the minimum fiber content to have filamentary strengthening of the composite material [4]. Additionally, ASTM D 4018 standard suggests typical resin mass fraction minimum of 0.6, which corresponds to a fiber volume fraction of 30% for HTR-40 in RTM 6. Thus a design targeted V_f of 34% was selected, which is roughly half of the high V_f in previous specimens and builds sufficient buffer against transverse compression. After factoring in mold machining tolerances, produced specimens had $V_f = 32\%$. The lack of transverse compression was evidenced by the preferential seating of low Vf fuzzy carbon fibers at the center of the composite specimen. From natural consolidation, dry fuzzy tow dimensions are thinner than the mold channel height, yielding a region of neat epoxy surrounding the tow (Figure 3.13).

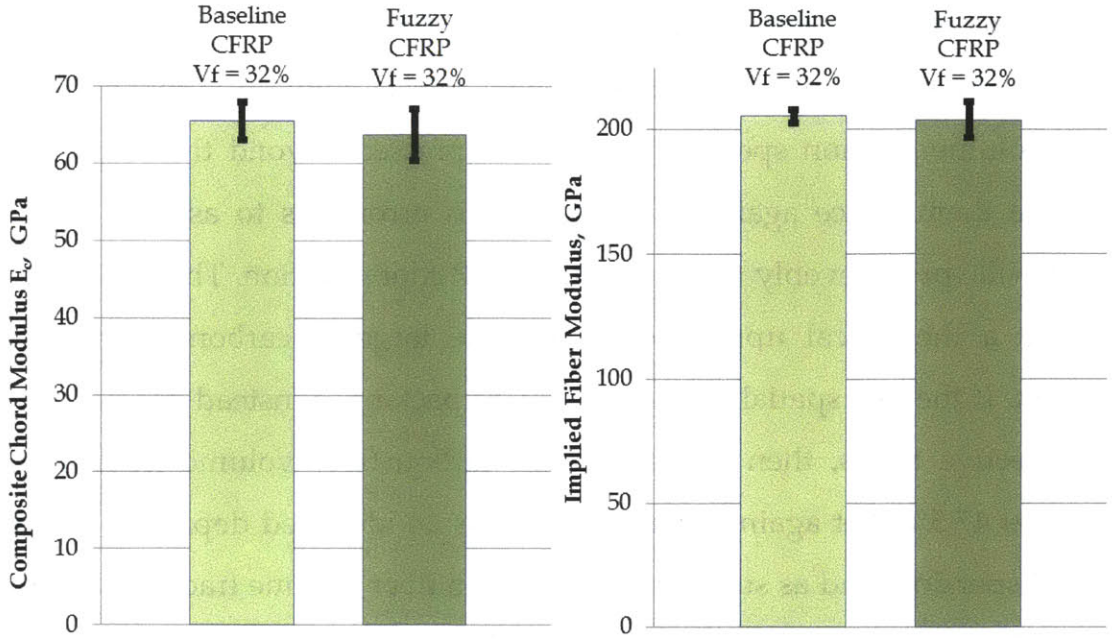

Figure 4.5 Low fiber volume fraction composite chord modulus (left) and implied fiber modulus (right) taken between 1000 and 6000 μstrain.

Utilizing the same methodology as before, composite and implied fiber modulus values could be determined for both low Vf baseline and fuzzy CFRP specimens. Composite modulus values of 65.4 ± 2.5 GPa (baseline) and 64 ± 3.4 GPa (fuzzy) closely match ROM predictions of 63 GPa. Implied fiber modulus results once again demonstrate that fuzzy carbon fibers retain elastic properties compared to baseline specimens. More importantly, both values match high Vf testing results, validating the consistency in this experimental method even with volume fractions changes.

Of more importance are the composite and implied fiber strength values for low Vf specimens. Surprisingly, baseline strengths were significantly lower than that of fuzzy CFRP as well as ROM predictions of 1.14 GPa. These value differences correlate with observed dissimilarities in failure between the specimens. Whereas low Vf baseline specimens exhibited very sudden

and brittle failures at low strains, fuzzy CFRP specimens formulated very visible matrix cracks on the specimen surface and continued to bear load. Interestingly, as load increased for the latter, more cracks would populate on the surface and saturate before reaching failure (Figure 4.7).

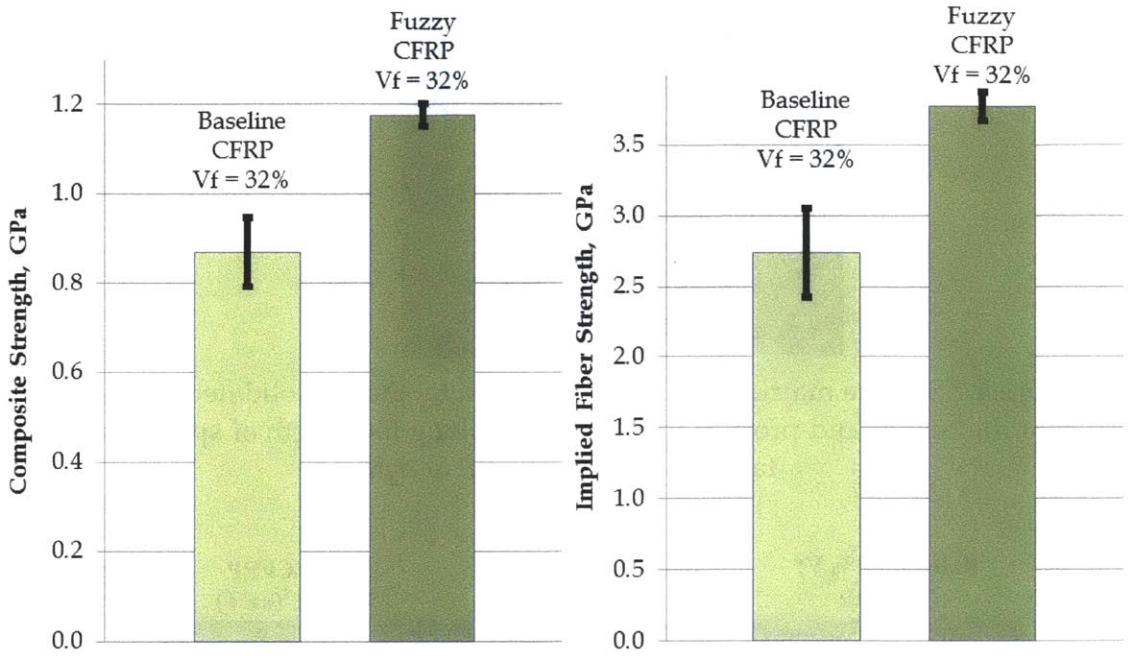

Figure 4.6 Low fiber volume fraction composite tensile strengths (left) and implied tensile strengths (right). Baseline strength values are low due to voids trapped within the tow during impregnation. On the other hand, fuzzy CFRP specimens were observed to deflect surface matrix cracks due to tow consolidation at the center of the composite specimen cross-section (see Figure 4.8).

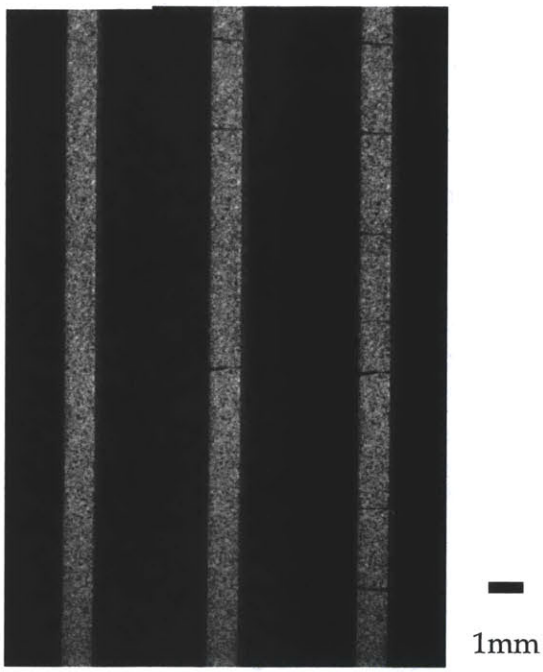

Figure 4.7 Surface matrix cracks were arrested by the consolidated fuzzy fiber tow at the center, and proceeded to populate along the length of specimen until failure *(in order from left to right)*

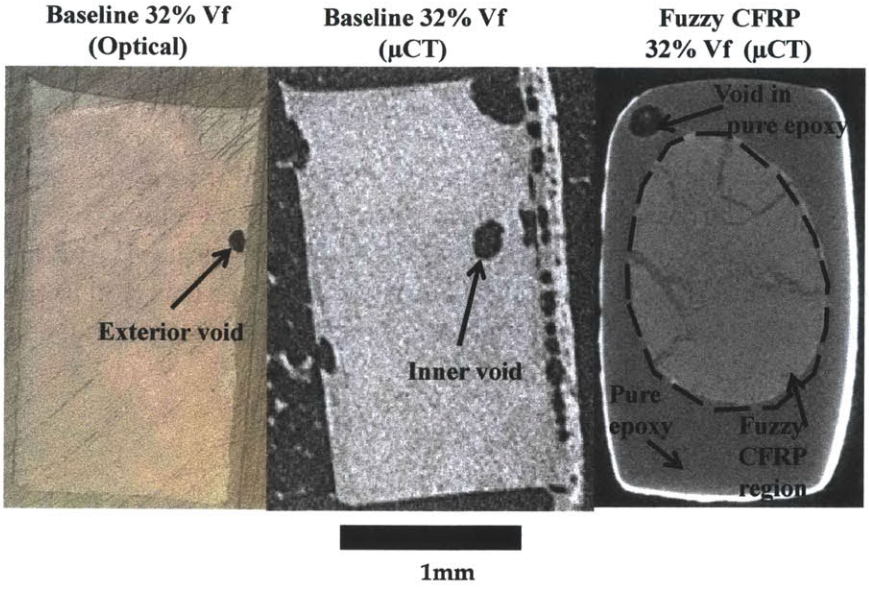

Figure 4.8 Low fiber volume fraction composite cross sectional views: Baseline under optical microscope showing the spread of fibers to fill the specimen cross section (left), baseline under micro-CT scan showing a void within the tow with a piece of tape adhered to the right of specimen (middle), and fuzzy CFRP under micro-CT showing fibers consolidated at the center with void formation in the resin-rich-region exterior to the tow.

To further understand the differences in the two failure behaviors, it is once again crucial to consider the distinctions in the tow seating and relative defect locations. Figure 4.8 shows representative cross sectional views of CFRP and fuzzy CFRP specimens obtained through optical microscopy and micro-CT scans. While multiple steps were taken to eliminate visible surface defects, voids were still present in both types of specimens. However, voids in fuzzy CFRP were found only exterior to the consolidated fiber tow (i.e., within the surrounding resin-rich regions), whereas voids in CFRP developed between fibers within the spread tow. Thus, upon high loading, matrix cracks that initiated from specimen surface defects were able to propagate inwards, but abruptly arrested by the fully impregnated fuzzy fiber tow at the center. In contrast, cracks initiated in baseline specimens were likely able to penetrate through fibers surrounding voids (subjected to higher stress intensities), and propagate catastrophically through the rest of the cross-section. Due to the defects internal to baseline fiber tows, low Vf CFRP strength values are not representative of the true pristine material strength, and are inaccurate for comparison with other strength values.

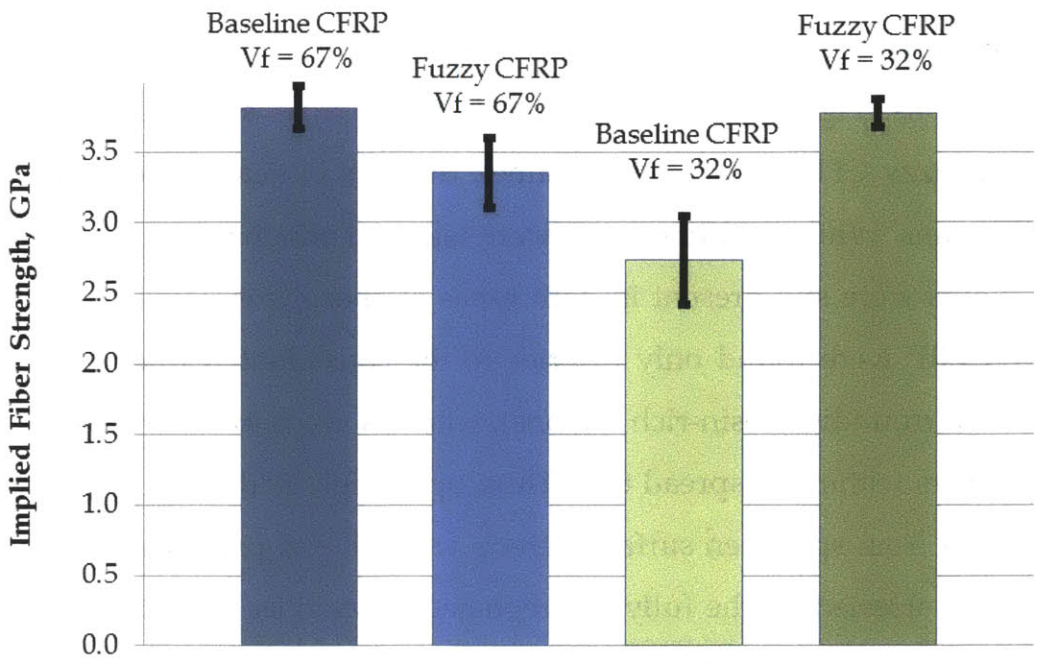

Figure 4.9 Implied fiber strength values indicate that undamaged low Vf fuzzy CFRP specimens have preserved fiber tensile strengths as those in high Vf baseline specimens.

However, because surface epoxy cracks were arrested in low Vf fuzzy CFRP specimens, final strength values are valid and reflect those of an intact impregnated fuzzy carbon fiber tow specimen at the core of the specimen, with a higher local Vf. A key finding here is that the implied fiber strengths of fuzzy carbon fibers are virtually the same as high Vf baseline strengths, indicating that HTR-40 fibers load-carrying capabilities are preserved -- consistent with single filament testing results. Thus, as hypothesized, fabricating lower Vf fuzzy CFRP without transverse compression-induced fiber damage results in preserved tensile properties, and suggests that the 12% loss in strength for 67% Vf fuzzy CFRP was attributed to molding procedures.

Chapter 5

Conclusions and Recommendations

Unidirectional fuzzy carbon fiber reinforced plastics (fuzzy CFRP) were successfully manufactured and tensile tested for the first time from carbon filaments (CF) with preserved strengths. Key contributions from this study are as follows:

- A scalable non-covalent functionalization technique was refined to improve CF wettability in CNT catalyst solution by achieving a thinner and conformal potassium polystyrene-*alt*-maleic anhydride (K-PSMA) coating.
- Tensioned vacuum heating and drying process of long dip-coated CF tows was developed, improving the consistency and morphology of high-yield radial CNT growth on CF.
- Fuzzy CFRP ply fabrication techniques at set fiber volume fractions were created via vacuum assisted resin infusion of fuzzy carbon fiber tows inside Teflon molds.
- Specimen tabbing procedures were established to prevent specimen pull-out and tab failures that would incur testing inaccuracies.

- Longitudinal elastic properties of fuzzy CFRP were found to be same as baseline CFRP specimens, and in direct alignment with micromechanical predictions that use previous single fiber testing data, thus validating the testing methodology and optical strain measurements.
- Fuzzy CFRP plies with preserved tensile strengths was demonstrated.

These advances bring to fruition fuzzy CFRPs that have the potential to improve interlaminar properties of CFRP without the compromise of in-plane tensile properties observed to date. Further, these efforts launch the research focus into exciting trajectories of specimen scale-up to coupon-level fuzzy CFRP laminates for aerospace applications.

An immediate first step in this direction is to transfer the presented incipient wetness technique and CNT growth processes onto aerospace grade carbon fiber weaves. Unsized fabrics are ideal substrates in order to maintain the similar graphitic surface chemistries as the research-grade HTR-40 fibers that were amenable to K-PSMA functionalization. If a consistent and innocuous desizing routine is implemented, sized weaves can also be investigated. Using existing experimental equipment, small dip-coated specimens can be subjected to the same low temperature thermal CVD script as before, and examined for CNT growth characteristics. An optimization of the K-PSMA coating/application may be necessary to ensure conformal and uniform CNT growth due to possible changes in wetting characteristics of a woven architecture [41].

Once desirable CNT morphologies are demonstrated on woven CF, scale-up to a larger CVD tube furnace will occur to process larger coated fabric.

Parametric studies surrounding gas flow rates, substrate placement locations, and temperature profiles will be conducted to eventually attain CNT coverage over the full specimen area and within tows, thereby making a full-scale fuzzy carbon fiber ply. Concurrently, a vacuum assisted resin infusion technique for these plies will be developed, leveraging existing in-house alumina FFRP manufacturing approaches.

The capability to make fuzzy CFRP laminates will enable a plethora of materials properties investigations as well as design opportunities for specific materials applications. Multifunctional properties such as electrical conductivity measurements will be more immediately attained via four point probe methods on initial fuzzy CFRP laminates. As fabrication techniques become more controlled, subsequent mechanical characterizations include manufacturing double cantilever beam and short beam shear specimens for measuring interlaminar fracture toughness and shear strength, respectively. Provided that tow seating and fiber waviness are not critically altered with radial CNT growth, open-hole tension and compression results of fuzzy CFRP laminates will be of direct relevance to aero-structures.

Additionally, the embedded network of highly conductive CNT within a fuzzy CFRP laminate may enable a host of integrated nondestructive evaluation methods as previously demonstrated for alumina-fiber FFRP. Specimens patterned with electrode grids can be tested to detect localized material resistance changes and identifying damaged regions [52] Likewise, enhanced thermography will be assessed on a fuzzy CFRP sample connected to a power source [53]. Subsequently, sensitivity experiments can further be conducted to tailor CNT growths for these damage-sensing capabilities. The vast array of laminate level characterization studies outlined above will not only benchmark fuzzy CFRP specimens, but also provide crucial mechanistic

understandings in order to further nano-engineer advanced composite solutions, and ultimately enable truly game-changing aerospace structures.

Appendix A

Table A.1 Summary of composite tensile properties from baseline CFRP and fuzzy CFRP fabricated at 67% and 32% V_f.

Specimen	Composite Chord Modulus (GPa)	Composite Chord Modulus Standard Deviation (GPa)	Composite Strength (GPa)	Composite Strength Standard Deviation (GPa)	Number of Samples Tested
67% Vf Baseline CFRP	134.7	5.0	2.59	0.12	5
67% Vf Fuzzy CFRP	137.7	6.5	2.25	0.19	4
32% Vf Baseline CFRP	65.4	2.5	0.87	0.08	5
32% Vf Fuzzy CFRP	63.6	3.4	1.18	0.02	4

Table A.2 Summary of implied fiber tensile properties from baseline CFRP and fuzzy CFRP fabricated at 67% and 32% V_f.

Specimen	Implied Fiber Modulus (GPa)	Implied Fiber Modulus Standard Deviation (GPa)	Implied Fiber Strength (GPa)	Implied Fiber Strength Standard Deviation (GPa)	Number of Samples Tested
67% Vf Baseline CFRP	198.3	5.0	3.81	0.15	5
67% Vf Fuzzy CFRP	205.4	4.0	3.35	0.25	4
32% Vf Baseline CFRP	205.4	2.7	2.74	0.31	5
32% Vf Fuzzy CFRP	203.9	7.3	3.77	0.10	4

Bibliography

[1] E. Garcia, B. Wardle, A. Johnhart, and N. Yamamoto, "Fabrication and multifunctional properties of a hybrid laminate with aligned carbon nanotubes grown In Situ," *Composites Science and Technology,* vol. 68, pp. 2034-2041, 2008.

[2] S. A. Steiner, 3rd, R. Li, and B. L. Wardle, "Circumventing the mechanochemical origins of strength loss in the synthesis of hierarchical carbon fibers," *ACS Appl Mater Interfaces,* vol. 5, pp. 4892-903, Jun 12 2013.

[3] H. Qian, A. Bismarck, E. S. Greenhalgh, G. Kalinka, and M. S. P. Shaffer, "Hierarchical composites reinforced with carbon nanotube grafted fibers: the potential assessed at the single fiber level," *Chemistry of Materials,* vol. 20, pp. 1862-1869, 2008.

[4] R. M. Jones, *Mechanics of composite materials* vol. 2: Taylor & Francis London, 1975.

[5] Hexcel, "HexTow AS4 Carbon Fiber Product Data," ed, 2013.

[6] S. G. Perron, "Passive Gust Load Alleviation Through Bend-Twist Coupling of Composite Beams on Typical Commercial Airplane Wings," S.M., AeroAstro, Massachussetts Institute of Technology, 2012.

[7] A. P. Mouritz, "Review of z-pinned composite laminates," *Composites Part A: Applied Science and Manufacturing,* vol. 38, pp. 2383-2397, 2007.

[8] L. Tong, A. P. Mouritz, and M. Bannister, *3D fibre reinforced polymer composites*: Elsevier, 2002.

[9] S. Iijima and T. Ichihashi, "Single-shell carbon nanotubes of 1-nm diameter," 1993.

[10] M.-F. Yu, O. Lourie, M. J. Dyer, K. Moloni, T. F. Kelly, and R. S. Ruoff, "Strength and breaking mechanism of multiwalled carbon nanotubes under tensile load," *Science*, vol. 287, pp. 637-640, 2000.

[11] J. Blanco, E. J. García, R. Guzmán de Villoria, and B. L. Wardle, "Limiting Mechanisms of Mode I Interlaminar Toughening of Composites Reinforced with Aligned Carbon Nanotubes," *Journal of Composite Materials*, vol. 43, pp. 825-841, April 1, 2009.

[12] N. Lachman and H. Daniel Wagner, "Correlation between interfacial molecular structure and mechanics in CNT/epoxy nano-composites," *Composites Part A: Applied Science and Manufacturing*, vol. 41, pp. 1093-1098, 2010.

[13] H. D. Wagner and A. Lustiger, "Optimized toughness of short fiber-based composites: The effect of fiber diameter," *Composites Science and Technology*, vol. 69, pp. 1323-1325, 2009.

[14] H. D. Wagner, P. M. Ajayan, and K. Schulte, "Nanocomposite toughness from a pull-out mechanism," *Composites Science and Technology*, vol. 83, pp. 27-31, 2013.

[15] N. Yamamoto, "Multi-scale electrical and thermal properties of aligned multi-walled carbon nanotubes and their composites," Massachusetts Institute of Technology, 2011.

[16] J. Qiu, C. Zhang, B. Wang, and R. Liang, "Carbon nanotube integrated multifunctional multiscale composites," *Nanotechnology*, vol. 18, p. 275708, 2007.

[17] A. Gohier, C. P. Ewels, T. M. Minea, and M. A. Djouadi, "Carbon nanotube growth mechanism switches from tip- to base-growth with decreasing catalyst particle size," *Carbon*, vol. 46, pp. 1331-1338, 2008.

[18] V. P. Veedu, A. Cao, X. Li, K. Ma, C. Soldano, S. Kar, *et al.*, "Multifunctional composites using reinforced laminae with carbon-nanotube forests," *Nat Mater*, vol. 5, pp. 457-462, 06//print 2006.

[19] S. S. Wicks, R. G. de Villoria, and B. L. Wardle, "Interlaminar and intralaminar reinforcement of composite laminates with aligned carbon nanotubes," *Composites Science and Technology,* vol. 70, pp. 20-28, 2010.

[20] S. S. Wicks, "Mechanical enhancement of woven composites with radially aligned carbon nanotubes (CNTs): investigation of Mode I fracture toughness," Massachusetts Institute of Technology, 2010.

[21] N. Yamamoto and B. Wardl, "Electrical and thermal properties of hybrid woven composites reinforced with aligned carbon nanotubes," in *Proceedings of the 49th AIAA/ASME/ASCE/AHS/ASC Structures, Structural Dynamics, and Materials Conference,* 2008.

[22] E. J. García, A. J. Hart, and B. L. Wardle, "Long carbon nanotubes grown on the surface of fibers for hybrid composites," *AIAA journal,* vol. 46, pp. 1405-1412, 2008.

[23] S. A. Steiner III, R. Li, R. Guzman de Villoria, M. S. Tsai, and B. L. Wardle, "Methods for Growing Carbon Nanotubes on Carbon Fibers that Preserve Fiber Tensile Strength," in *Proceedings of the 51st AIAA Structures, Structural Dynamics, and Materials (SDM) Conference,* 2010, pp. 12-15.

[24] Q. Zhang, J. Liu, R. Sager, L. Dai, and J. Baur, "Hierarchical composites of carbon nanotubes on carbon fiber: Influence of growth condition on fiber tensile properties," *Composites Science and Technology,* vol. 69, pp. 594-601, 2009.

[25] R. J. Sager, P. J. Klein, D. C. Lagoudas, Q. Zhang, J. Liu, L. Dai, *et al.*, "Effect of carbon nanotubes on the interfacial shear strength of T650 carbon fiber in an epoxy matrix," *Composites Science and Technology,* vol. 69, pp. 898-904, 2009.

[26] T.-W. Chou, L. Gao, E. T. Thostenson, Z. Zhang, and J.-H. Byun, "An assessment of the science and technology of carbon nanotube-based fibers and composites," *Composites Science and Technology,* vol. 70, pp. 1-19, 2010.

[27] J. N. Coleman, U. Khan, W. J. Blau, and Y. K. Gun'ko, "Small but strong: A review of the mechanical properties of carbon nanotube–polymer composites," *Carbon,* vol. 44, pp. 1624-1652, 2006.

[28] K. L. Kepple, G. P. Sanborn, P. A. Lacasse, K. M. Gruenberg, and W. J. Ready, "Improved fracture toughness of carbon fiber composite functionalized with multi walled carbon nanotubes," *Carbon*, vol. 46, pp. 2026-2033, 2008.

[29] M. T. Fahey, "Nonlinear and Anisotropic Behavior of High Performance Fibers," Massachusetts Institute of Technology, 1993.

[30] A. Carrillo, J. A. Swartz, J. M. Gamba, R. S. Kane, N. Chakrapani, B. Wei, *et al.*, "Noncovalent Functionalization of Graphite and Carbon Nanotubes with Polymer Multilayers and Gold Nanoparticles," *Nano Letters*, vol. 3, pp. 1437-1440, 2003/10/01 2003.

[31] A. Magrez, J. W. Seo, R. Smajda, B. Korbely, J. C. Andresen, M. Mionić, *et al.*, "Low-Temperature, Highly Efficient Growth of Carbon Nanotubes on Functional Materials by an Oxidative Dehydrogenation Reaction," *ACS Nano*, vol. 4, pp. 3702-3708, 2010/07/27 2010.

[32] ASTM, "Standard Test Method for Tensile Strength and Young's Modulus for High-Modulus Single-Filament Materials," vol. D 3379 - 75, ed, 1989.

[33] S. A. Steiner III, "Carbon nanotube growth on challenging substrates: applications for carbon-fiber composites," Massachusetts Institute of Technology, 2011.

[34] M. S. Dresselhaus, G. Dresselhaus, and K. Sugihara, *Graphite fibers and filaments* vol. 5: Springer-Verlag Berlin, 1988.

[35] A. D. Stroock, R. S. Kane, M. Weck, S. J. Metallo, and G. M. Whitesides, "Synthesis of Free-Standing Quasi-Two-Dimensional Polymers," *Langmuir*, vol. 19, pp. 2466-2472, 2003/03/01 2002.

[36] N. Yamamoto, A. John Hart, E. J. Garcia, S. S. Wicks, H. M. Duong, A. H. Slocum, *et al.*, "High-yield growth and morphology control of aligned carbon nanotubes on ceramic fibers for multifunctional enhancement of structural composites," *Carbon*, vol. 47, pp. 551-560, 2009.

[37] ISO, "ISO 10618 Carbon fibre - Determination of tensile properties of resin-impregnated yarn," 8/15/2004 2004.

[38] SACMA, "SACMA Recommended Method for Tow Tensile Testing of Carbon Fibers," ed, 1994.

[39] ASTM, "D4018 - 99 Standard Test Methods for Properties of Continuous Filament Carbon and Graphite Fiber Tows," ed, 2008.

[40] Hexcel, "HexFlow RTM 6 Product Data," 2007.

[41] S. S. Wicks, "Manufacturability of Hybrid Aligned Carbon Nanotube (CNT)-Fiber Composites Through Vacuum Assisted Resin Infusion As Dependent On CNT Loading," in *24th Advanced Aerospace Materials and Processes (AeroMat) Conference and Exposition*, 2013.

[42] K. Magniez, A. Vijayan, and N. Finn, "Apparent volumetric shrinkage study of RTM6 resin during the curing process and its effect on the residual stresses in a composite," *Polymer Engineering & Science,* vol. 52, pp. 346-351, 2012.

[43] T. S. Lundström and B. R. Gebart, "Influence from process parameters on void formation in resin transfer molding," *Polymer Composites,* vol. 15, pp. 25-33, 1994.

[44] N. Patel and L. J. Lee, "Modeling of void formation and removal in liquid composite molding. Part II: Model development and implementation," *Polymer Composites,* vol. 17, pp. 104-114, 1996.

[45] H. J. Barraza, Y. K. Hamidib, L. Aktasb, A. Edgar, and M. Altan, "Porosity reduction in the high-speed processing of glass-fiber composites by resin transfer molding (RTM)," *Journal of composite materials,* vol. 38, pp. 195-226, 2004.

[46] D. Handlin, R. Guzmán de Villoria, S. H. Chan, H. Cebeci, M. Williams, E. Parsons, *et al.*, "Three-Dimensional Constitutive Relations of Aligned Carbon Nanotube Polymer Nanocomposites," 2013.

[47] S. I. Kundalwal and M. C. Ray, "Micromechanical analysis of fuzzy fiber reinforced composites," *International Journal of Mechanics and Materials in Design,* vol. 7, pp. 149-166, 2011/06/01 2011.

[48] H. Cebeci, H. S. Türkmen, and B. L. Wardle, "Mechanical Behaviour Of Waviness-Dominated Controlled Morphology Aligned Carbon Nanotube

Polymer Composites: Modeling Study Correlated With Experiments," in *18th International Conference On Composite Materials*, Korea.

[49] A. A. Griffith, "The phenomena of rupture and flow in solids," *Philosophical transactions of the royal society of london. Series A*, vol. 221, pp. 163-198, 1921.

[50] S. V. Hoa, in *Principles of the manufacturing of composite materials*, ed: DEStech Publications, Inc, 2009, p. 29.

[51] D. Hull and T. W. Clyne, "Geometrical aspects," in *An introduction to composite materials*, ed Great Britain: Cambridge University Press, 1981, pp. 59-80.

[52] S. Wicks, R. Guzman de Villoria, A. Raghavan, S. Kessler, and B. Wardle, "Tomographic Electrical Resistance-based Damage Sensing in Nano-Engineered Composite Structures," presented at the 51st AIAA/ASME/ASCE/AHS/ASC Structures, Structural Dynamics, and Materials Conferenc, Orlando, FL, 2010.

[53] R. Guzmán de Villoria, N. Yamamoto, A. Miravete, and B. L. Wardle, "Multi-physics damage sensing in nano-engineered structural composites," *Nanotechnology*, vol. 22, p. 185502, 2011.